Article

NET4 and RabG3 link actin to the tonoplast and facilitate cytoskeletal remodelling during stomatal immunity

Timothy J. Hawkins[1,7], Michaela Kopischke [2,3,7], Patrick J. Duckney[1,7], Katarzyna Rybak[3], David A. Mentlak [1], Johan T. M. Kroon [1], Mai Thu Bui[4], A. Christine Richardson [1], Mary Casey[2], Agnieszka Alexander[2], Geert De Jaeger[5], Monika Kalde[6], Ian Moore[6], Yasin Dagdas [4], Patrick J. Hussey [1] ✉ & Silke Robatzek [2,3] ✉

Members of the NETWORKED (NET) family are involved in actin-membrane interactions. Here we show that two members of the NET family, NET4A and NET4B, are essential for normal guard cell actin reorganization, which is a process critical for stomatal closure in plant immunity. NET4 proteins interact with F-actin and with members of the Rab7 GTPase RABG3 family through two distinct domains, allowing for simultaneous localization to actin filaments and the tonoplast. NET4 proteins interact with GTP-bound, active RABG3 members, suggesting their function being downstream effectors. We also show that RABG3b is critical for stomatal closure induced by microbial patterns. Taken together, we conclude that the actin cytoskeletal remodelling during stomatal closure involves a molecular link between actin filaments and the tonoplast, which is mediated by the NET4-RABG3b interaction. We propose that stomatal closure to microbial patterns involves the coordinated action of immune-triggered osmotic changes and actin cytoskeletal remodelling likely driving compact vacuolar morphologies.

The NETWORKED (NET) family of proteins are key molecular components of actin-membrane interactions in plants[1,2]. As such, they directly bind to the actin cytoskeleton and localise to membrane compartments. Different NET proteins link actin to specific membranes, including actin-vacuole interactions (NET4A), actin-nuclear membrane interactions (NET3A), actin-plasma membrane (PM) interactions (NET2A), actin-plasmodesmata interactions (NET1A), actin-endoplasmic reticulum (ER) interactions (NET3B), and actin-PM/ER contact site (EPCS) interactions (NET3C)[1,3,4]. These actin-membrane interactions are thought to influence actin dynamics and membrane morphology, responsible for controlling root and pollen tube development, cell expansion and pavement cell morphogenesis[1,5–7].

Underpinning these processes are interactions of NET proteins with other proteins to form complexes that could be tissue or developmental stage specific, overlapping with the expression patterns of the *NET* genes. For example, NET2A is expressed specifically in pollen and forms a complex with the transmembrane POLLEN RECEPTOR-LIKE KINASES (PRK) 4 and 5, indicating that NET proteins could link external signalling events with actin-membrane dynamics[5]. NET3C exists in complexes with VAP27, KINESIN-LIGHT-CHAIN-RELATED (KLCR) and calmodulin-binding IQ67 DOMAIN (IQD) proteins, which

[1]Department of Biosciences, University of Durham, South Road, Durham DH1 3LE, UK. [2]The Sainsbury Laboratory, Norwich Research Park, Norwich NR4 7UH, UK. [3]LMU Munich Biocenter, Großhadener Strasse 4, 82152 Planegg, DE, Germany. [4]Gregor Mendel Institute (GMI), Austrian Academy of Sciences, Vienna BioCenter, Vienna, AUT, Austria. [5]VIB-University Ghent, Center for Plant System Biology, Technologiepark 927, 9052 Ghent, BE, Belgium. [6]Department of Plant Sciences, University of Oxford, South Parks Rd., Oxford OX1 3RB, UK. [7]These authors contributed equally: Timothy J. Hawkins, Michaela Kopischke, Patrick J. Duckney. ✉e-mail: p.j.hussey@durham.ac.uk; robatzek@bio.lmu.de

mediate the interaction between actin, microtubules and ER at the EPCS[7,8]. It is thus possible that EPCS represent focal points of signal sensing and cytoskeletal organization. Given their link to the cytoskeleton and specific lipid and protein composition, EPCS could also have roles in membrane trafficking, i.e. endocytosis and/or autophagy[2,9].

Both NET1A and NET4A are predominantly expressed in the root meristem and elongation zone[1]. However, NET1A and NET4A localize to distinct membranes, the plasmodesmata and the vacuole respectively, and therefore they likely control actin-membrane dynamics in different plant processes. NET1A is involved in root development but the process regulated by NET4A remains unknown[1]. Given that NET4A localizes to the vacuole, it is interesting to note that cells of the root meristem and elongation zone are characterized by complex vacuolar structures, i.e. fragmented and/or with tubular morphology[10]. Only recently it was reported in roots that NET4A appears to have a stronger vacuolar localization in the centre of the cell, a region of higher vacuolar constrictions. Knock-out mutants of NET4A and its closest homologue NET4B, and NET4A overexpression result in more spherical vacuoles[11].

Morphological dynamics of vacuoles are not only involved in plant growth but are a hallmark of stomatal movements[12]. The vacuoles in the two guard cells that form the stomatal pore change their volume and size, driving the closure and opening of the pore. When stomata close, the vacuole morphology becomes more complex with invaginations and bulb-like structures in the lumen, increasing the total vacuole surface area by 20%[12]. These intra-vacuolar structures could represent a storage of excess membrane material during stomatal closure.

Actin filament dynamics are associated with stomatal movements, forming distinct actin arrays within guard cells: radial orientation in open stomata and a longitudinal orientation in closed stomata[13]. Actin filaments transiently bundle during stomatal opening but bundles dissolve when stomata are fully open. Consequently, chemical interference with actin dynamics affects stomatal movements. Blocking actin polymerization with Cytochalasin D promotes light-induced stomatal opening, while Latrunculin B promotes abscisic acid (ABA)-induced stomatal closure[14,15]. Stabilizing actin with Phalloidin and Jasplakinolide inhibits ABA-induced stomatal closing[15]. Genetic disruption of actin bundling, i.e. upon overexpression of the ACTIN DEPOLYMERIZATION FACTOR 1 (ADF1) or inactivation of the small GTPase AtRac1 induces stomatal closure[16,17].

Guard cells respond to numerous physiological and environmental cues, including stomatal closure induced upon drought stress and pathogen attack[18]. Thus, signalling events are likely impacting on guard cell actin dynamics. Perception of pathogen-associated molecular patterns (PAMPs) such as bacterial flagellin and fungal chitin closes stomata and thereby protect against pathogen invasion[18]. The cognate receptor for flagellin and its derived peptide flg22 is FLAGELLIN SENSING 2 (FLS2), which is highly expressed in guard cells[19,20]. Ligand-activation of the FLS2 – BRASSINOSTEROID INSENSITIVE 1-ASSOCIATED RECEPTOR KINASE 1 (BAK1) receptor complex induces signalling cascades resulting in the phosphorylation of the RESPIRATORY BURST OXIDASE HOMOLOG PROTEIN D (RBOHD) NADPH oxidase, S-type anion channel SLOW ANION CHANNEL1 (SLAC1) and its homologue SLAH3, required for PAMP-triggered stomatal closure[21,22].

Additionally, flg22 perception results in a rapid change in the higher ordered state of the actin filament array within the guard cell, mostly showing radial array and radial bundles during the treatment[13]. Epidermal pavement cells show increased actin filament abundance in response to flg22 and chitin in a FLS2, CHITIN ELICITOR RECEPTOR KINASE1 (CERK1) and ADF4-dependent manner[23,24]. Likewise, guard cell actin filament orientation and density changed upon flg22-induced stomatal closure. MPK3/6-mediated phosphorylation of VILLIN3 (VLN3) facilitates the disassembly of radial actin arrays, initiating the

reorganization of actin filaments and thereby ensuring proper flg22-induced stomatal closure[25]. Whether actin-membrane interaction, such as NET4A-mediated actin-vacuole tethering, play roles in PAMP-induced immune responses, including stomatal closure, remains to be determined.

In this work, we examined NET4A and its closest homologue NET4B. They both localized to actin filaments and the tonoplast. Expression studies and phenotypic analysis of knock-out mutants revealed a role for both of the NET4 proteins in stomatal closure to flg22, indicative of their similar function. The net4 mutants exhibit impaired stomatal closure at long treatment times but at earlier time points they were not immune-compromised. Using a combination of yeast-two-hybrid (Y2H), co-immunoprecipitation and FRET-FLIM assays, we show that the NET4 proteins form homo- and hetero-dimeric complexes, and interact with members of the RABG3 family. We also demonstrate that rabg3b mutants, but not mutants in other RABG3 genes, are specifically impaired in robust flg22-induced stomatal closure, phenocopying the two net4 mutants. Analysis of the subcellular function of NET4 and RABG3 using the net4 and rabg3b mutants suggest that the couple is involved in the reorganisation of the actin cytoskeleton, likely facilitating compact vacuolar morphologies. In addition, our data support a model of the two NET4 proteins being RABG3B effectors.

Results

NET4 proteins localize to actin filaments and the tonoplast

Previous work suggested NET4A localizing to the actin cytoskeleton and the vacuole[1,11,26]. We further defined the subcellular localization of NET4A. Confocal microscopy of stable transgenic *Arabidopsis thaliana* lines expressing NET4A-GFP under its native promoter exhibited detectable signals in roots and revealed a striking filamentous network pattern of NET4A-GFP (Fig. 1a). Co-expression with the actin marker Lifeact-RFP confirmed the localization of NET4A-GFP to the actin cytoskeleton (Fig. 1a). Detailed inspection showed discrete NET4A-GFP punctae labelling along the Lifeact-RFP actin filaments (Fig. 1a; Supplementary Movie 1), a characteristic "beads-on-a-string" localization similar to other members of the NET family[1]. Furthermore, analysis of transgenic Arabidopsis lines co-expressing native promotor-driven NET4A-GFP and the well-established tonoplast marker RABG3f-mCherry showed that NET4A localizes at the tonoplast (Fig. 1b, c; Supplementary Movies 2, 3)[27].

Since NET4B-GFP expression was below the detection limit in stable transgenic Arabidopsis lines, we studied its localization in *Nicotinana benthamiana*. Transient expression of NET4B-GFP showed patterns reminiscent of NET4A-GFP and co-localization with the actin marker FABD2-mCherry (Supplementary Fig. 1a). A hallmark of NET family proteins is the NET actin-binding (NAB) domain[1]. To corroborate that the observed association of NET4B with actin represents direct binding to microfilaments, we mixed the recombinant NET4B 6xHIS-NAB domain with purified actin in a co-sedimentation assay. Upon ultracentrifugation, 6HIS-NET4B[1-105] co-sedimented in the presence of F-actin, proving a direct association between NET4B and microfilaments (Supplementary Fig. 1b). Using an isotype-specific anti-NET4B antibody and immuno-gold labelling, we detected enriched signals in close proximity to tonoplast structures of lytic vacuoles by transmission electron microscopy (Supplementary Fig. 1c). Taken together, we conclude that NET4 proteins directly bind actin through the NAB domain and at the same time associate with the tonoplast. This simultaneous localization pattern is consistent with the role of NET family proteins as actin-membrane tethers.

Being close homologues and exhibiting the same localization patterns, we hypothesized that NET4A and NET4B could co-localize and interact with each other. Concordantly, confocal microscopy of NET4A-GFP and NET4B-RFP in *N. benthamiana* revealed their co-localization, observed as actin cytoskeleton patterns (Fig. 2a).

Consistently, we found that both NET4A and NET4B can form homo- and heterodimers in yeast (Fig. 2b), and *in planta* (Fig. 2c). FRET-FLIM analysis of co-expressing NET4A-GFP and NET4B-RFP *N. benthamiana* leaves confirmed this interaction through the significant reduction in donor lifetime (Fig. 2d, e).

NET4 proteins are required for proper stomatal closure to flg22
To gain insights into the plant processes, which could be regulated by NET4A and NETB, we evaluated their transcriptional expression patterns using stable promoter GUS lines in *A. thaliana*. As shown in Fig. 3, we observed clear GUS signals in roots across cell files and developmental zones for both promoters (Fig. 3a, b). This is in

agreement with the previously reported expression of NET4A-GFP in root epidermal cells[1,11,27]. In addition, we found GUS expression in trichomes conferred by the *NET4A* promoter and in guard cells by the *NET4B* promoter (Fig. 3a, b, Supplementary Fig. 1d). To validate *NET4* guard cell expression, we performed qRT-PCR analysis and found a high expression of *NET4B* but not *NET4A* in guard cell enriched samples compared to mesophyll cells (Fig. 3c). Analysis of AtGenExpress and GEO microarray experiment data confirmed *NET4B* expression in guard cells and revealed transcriptional responsiveness to flg22 and bacterial infection (*NET4A* is not available on the Affymetrix Arabidopsis ATH1 genome array used in these experiments).
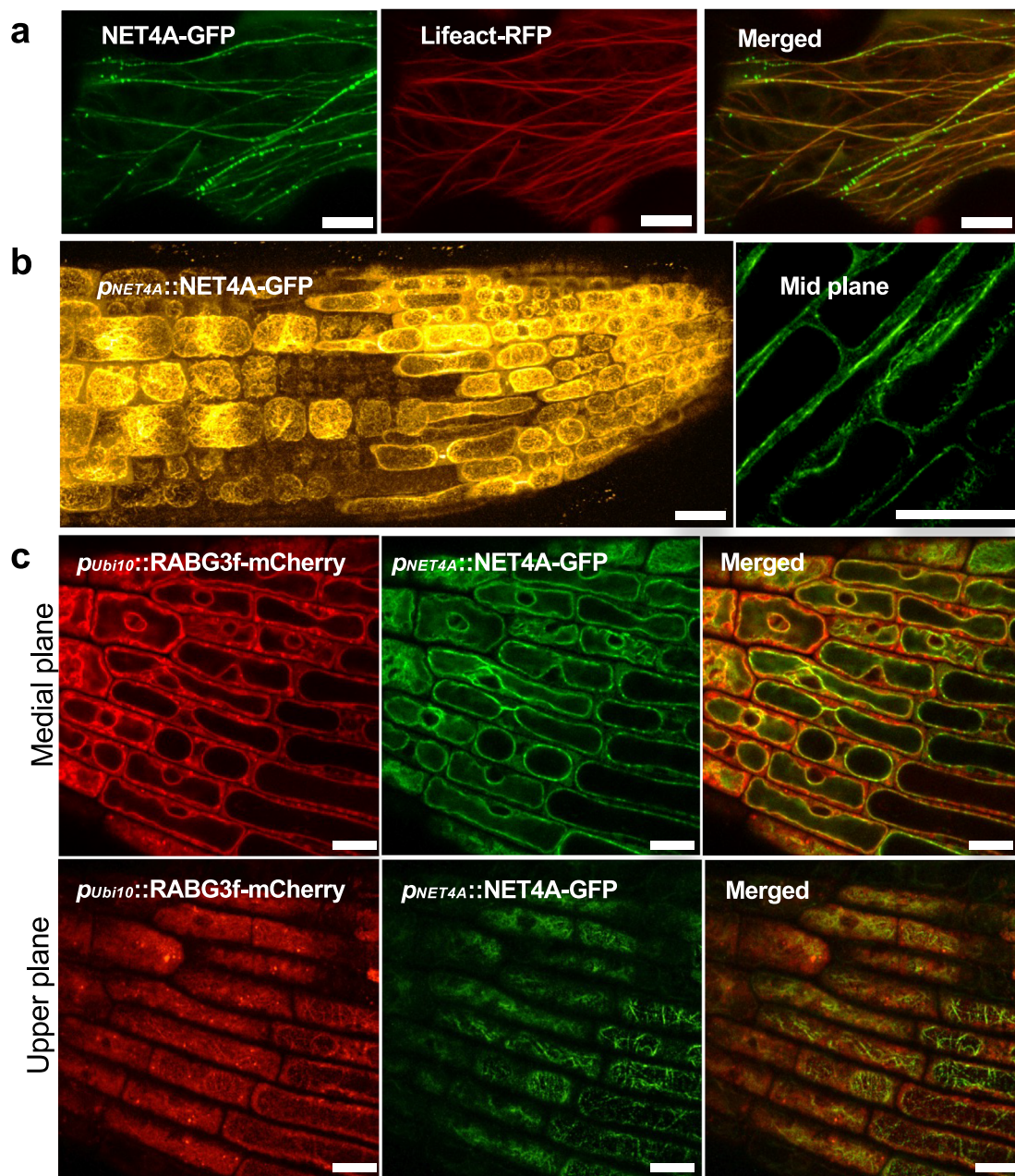

Fig. 1 | NET4 proteins decorate actin filaments and localise to the tonoplast.
a Confocal microscopy of *N. benthamiana* leaves transiently expressing NET4A-GFP and Lifeact-RFP; scale bars = 10 μm. **b** Confocal microscopy of transgenic Arabidopsis lines expressing NET4A-GFP under its native promoter. NET4A-GFP localises to filaments and the tonoplast membrane; scale bars = 20 μm. **c** Confocal microscopy of transgenic Arabidopsis lines co-expressing *pNET4A*::NET4A-GFP and pUbi10::mCherry-RABG3f. NET4A-GFP and mCherry-RABG3f co-localise at the tonoplast in planta; scale bars = 10 μm. All experiments were repeated at least thrice with similar results.
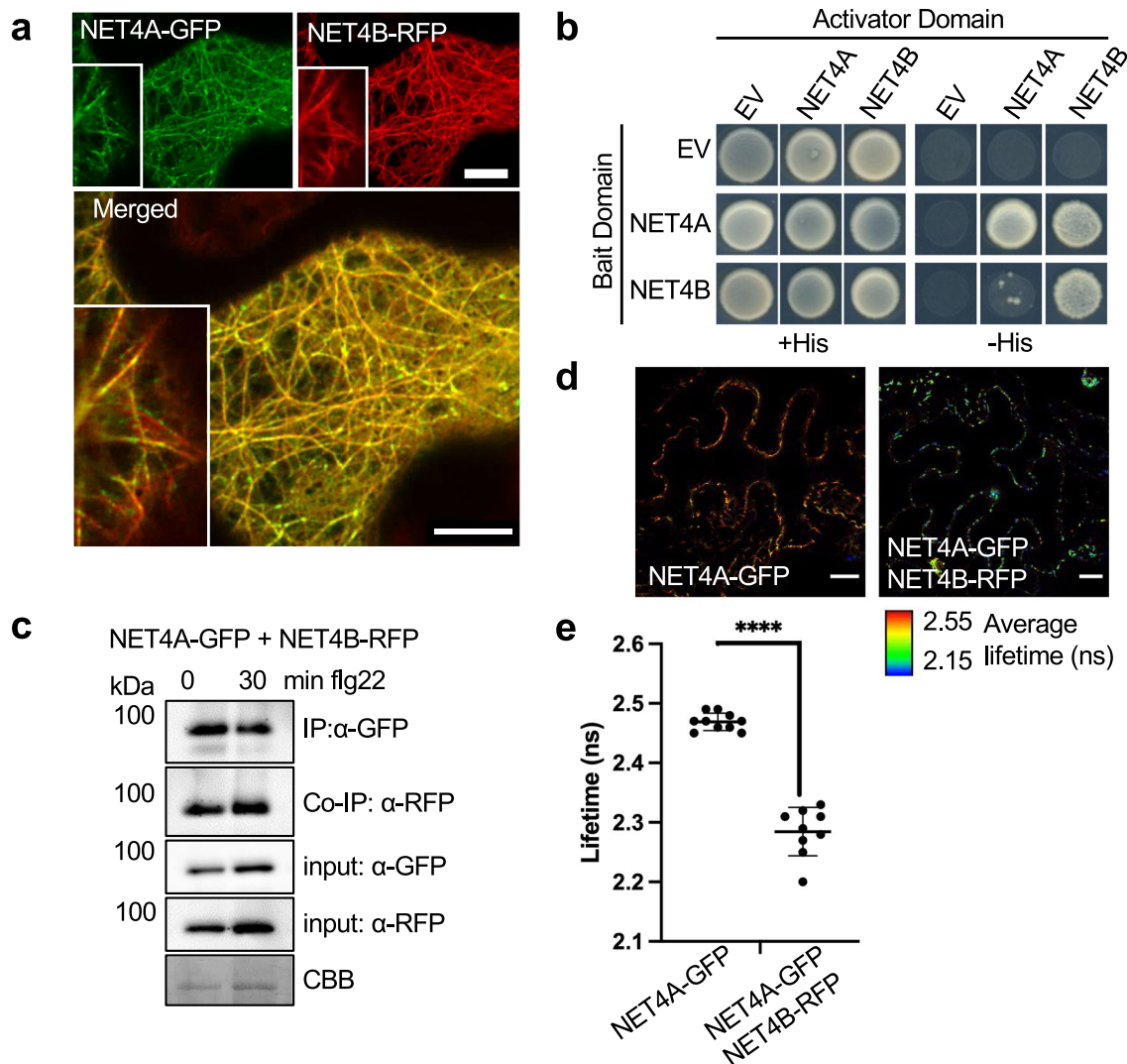
Fig. 2 | NET4 proteins co-localize, interact with each other and themselves.
a Confocal micrographs of *N. benthamiana* leaf epidermal cells transiently co-expressing NET4A-GFP and NET4B-RFP. Shown are single plane confocal images capturing GFP fluorescence (green), RFP fluorescence (red) and overlaid signals (yellow); scale bars = 20 μm. The experiment was repeated at least thrice with similar results. **b** Yeast-two-hybrid analysis of the indicated constructs indicate homo- and heterodimer interactions of NET4A and NET4B (EV = empty vector). The experiment was repeated at least thrice with similar results. **c** Co-immunoprecipitation (Co-IP) assay of NET4A-GFP with NET4B-RFP. Fusion proteins were co-expressed in *N. benthamiana*, immunoprecipitated (IP) using GFP-trap beads and detected using fluorophore fusion specific antibodies (GFP and RFP). 1% of the input is shown as loading control. Blots are representative of two independent experiments. **d** FRET-FLIM analysis of NET4A-GFP and NET4B-RFP interaction. FLIM (TCSPC) confocal images of *N. benthamiana* leaf epidermal cells co-expressing both NET4 proteins. Data shown using lifetime LUT. **e** Graph of fluorescence lifetime values of donor alone and donor + acceptor. The significant reduction in lifetime of the donor in the presence of the acceptor indicates energy transfer and a physical interaction; $n = 10$, $p < 0.0001$ Mann Whitney *t*-test; errors bars represent SD. The experiment was repeated at least twice with similar results.

Next, we isolated T-DNA insertional lines for both *NET4* genes resulting in loss-of-function of *NET4A* and knock-down of *NET4B*, selected *net4a* x *net4b* double mutants from single line crosses and generated two *net4ab* double null mutants using CRISPR-Cas (*net4ab-c1* and *net4ab-c2*), used for phenotype characterization (Supplementary Fig. 2a, b). Although previous works point at roles for NET4A and NET4B in vacuole morphology in roots[11], we did not observe obvious defects in plant growth and development (Supplementary Fig. 2c). Because previous work identified that stomatal guard cell actin filament organization is altered in response to flg22[25,28], we focussed our phenotype analysis on stomatal behaviours. Single and double *net4a* and *net4b* mutants exhibited impaired stomatal closure to flg22 but not ABA (Fig. 3d, e), suggesting a specific impairment in pattern-triggered immunity (PTI). However, *net4* mutants were not generally immune-compromised, showing wild type-like production of reactive oxygen species (ROS)

and activation of mitogen-activated protein kinases (MAPKs) (Fig. 3f, g), two typical PTI responses and ROS being required for stomatal closure[18,21]. Since we observed a slight increase in MAPK activation at 120 min flg22 elicitation in *net4a* mutants, we monitored flg22-induced ROS production over a longer time, and this was wild type-like in the mutants (Supplementary Fig. 2d). The slight increase in MAKP activation at 120 min flg22 elicitation in *net4a* mutants may suggest roles for NET4 proteins at later PTI responses compared with the ROS burst, for example. NET4A and NET4B do not appear to be required for the prototypic PTI oxidative burst and early MAPK activation, and thus rather could be involved in guard cell-specific PTI signalling and/or other cellular aspects of stomatal closure. Consistently, *net4ab-c2* double mutants supported increased growth of the non-virulent *Pseudomonas syringae pv. tomato* DC3000 (Pto DC3000) *Hrc-* strain, whereas bacterial growth was found to be similar in Col-0 and *net4ab-c2* double mutants when
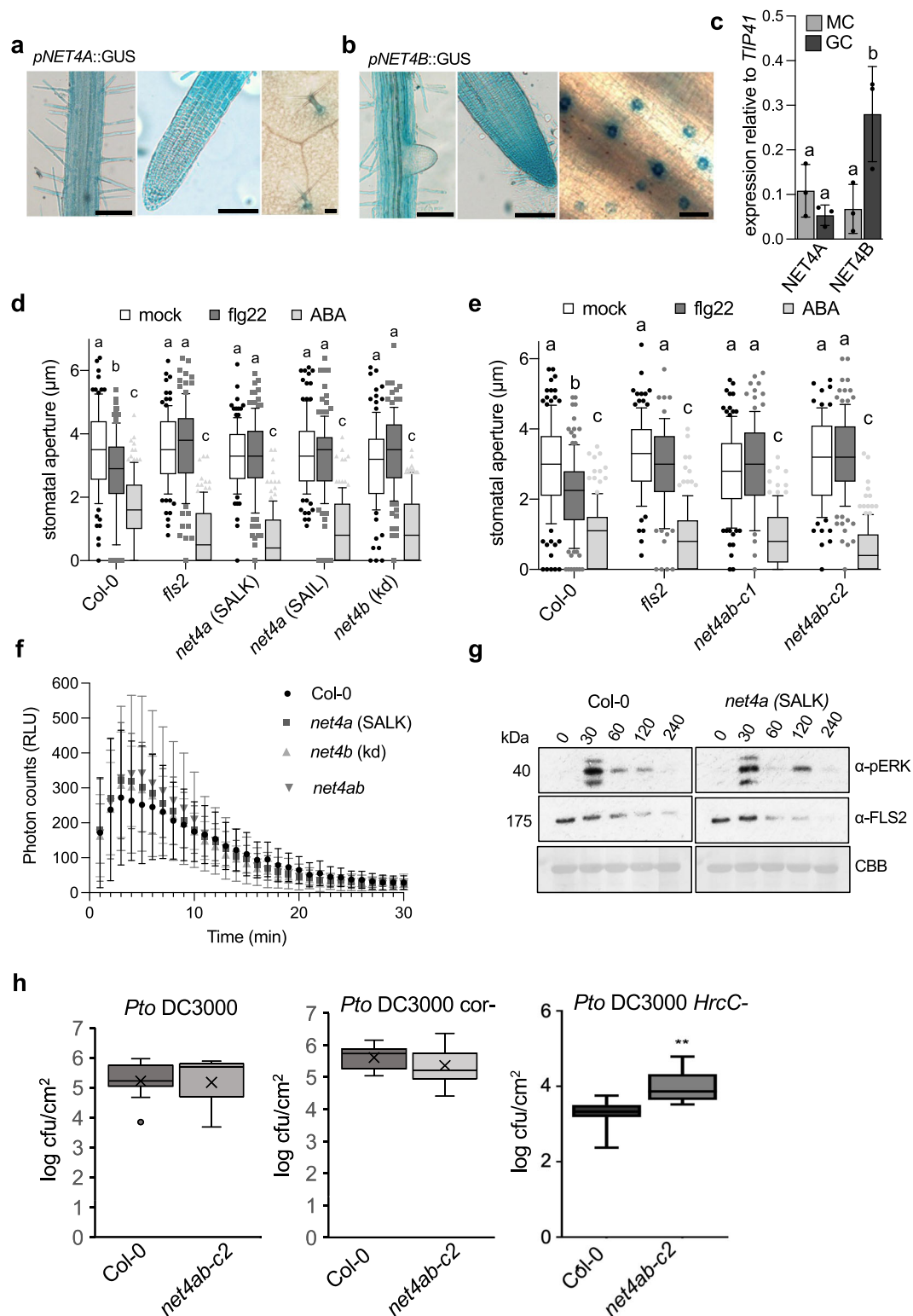
infected with *Pto* DC3000 wild type and the coronatine-defective *Pto* DC3000 cor- strain (Fig. 3h).

NET4 proteins behave like downstream effectors of RABG3 GTPases

To further identify functions of NET4A and NET4B, we screened for interacting proteins using tandem-affinity purification followed by mass-spectrometry analysis (Supplementary Table 1). In yeast, both, NET4A and NET4B interacted with members of the RABG3 family, including RABG3a and RABG3f (Fig. 4a). Multiple members of the RABG3 class localise to the tonoplast and have roles in vacuolar trafficking and fusion[26,29]. Therefore, we focused on RABG3 family proteins as interactors of NET4A and NET4B. We validated their interaction *in planta*, detecting association of NET4B with YFP-RABG3f in

Fig. 3 | *net4* mutants are impaired in flg22- but not ABA-induced stomatal closure and other PTI responses. a, b GUS-stained tissues of stable transgenic Arabidopsis *NET4A* and *NET4B* promoter-driven GUS reporter line seedlings. Scale bars (a) = 100 μm (right), 100 μm (middle), 50 μm (left); scale bars (b) = 100 μm (right), 100 μm (middle), 20 μm (left). The experiments were repeated at least thrice with similar results. **c** Transcript levels of *NET4A* and *NET4B* were quantified in guard cells (GC)-enriched samples or whole cell samples (MC), respectively, relative to *TIP41*. Bars represent mean values ± SEM of 3 replicates (ANOVA with Bonferroni's Multiple Comparison Test). Different letters indicate significantly different values at *p* < 0.05. The experiment was repeated twice with similar results. **d, e** Stomatal aperture measurements in *net4a* and *net4b* single and *net4ab-c1 and -c2* CRISPR-Cas double mutants compared with Col-0 and *fls2*. Stomatal apertures measured 2 h after treatment with 20 μM flg22 and 10 μM ABA. Box plots of the values are shown with whiskers from the 5th to 95th percentiles, the line in the box shows the median (**d**: Col-0 (mock) *n* = 93 stomata, Col-0 (flg22) *n* = 115, Col-0 (ABA) *n* = 114, *fls2* (mock) *n* = 100, *fls2* (flg22) *n* = 102, *fls2* (ABA) *n* = 112, *net4a* SALK (mock) *n* = 118, *net4a* SALK (flg22) *n* = 128, *net4a* SALK (ABA) *n* = 125, *net4a* SAIL (mock) *n* = 115, *net4a* SAIL (flg22) *n* = 126, *net4a* SAIL (ABA) *n* = 124, *net4b* kd (mock) *n* = 105, *net4b* kd (flg22) *n* = 107, *net4b* kd (ABA) *n* = 120; **e**: Col-0 (mock) *n* = 131 stomata,

Col-0 (flg22) *n* = 124, Col-0 (ABA) *n* = 123, *fls2* (mock) *n* = 123, *fls2* (flg22) *n* = 92, *fls2* (ABA) *n* = 128, *net4ab-c1* (mock) *n* = 113, *net4ab-c1* (flg22) *n* = 115, *net4ab-c1* (ABA) *n* = 110, *net4ab-c2* (mock) *n* = 83, *net4ab-c2* (flg22) *n* = 124, *net4ab-c2* (ABA) *n* = 133 stomata. Different letters indicate significantly different values at *p* < 0.0001 (2-way ANOVA, multiple comparisons). Both experiments were repeated twice with similar results. **f** ROS production measured as relative luminescence units (RLU) in the indicated genotypes treated with 100 nM flg22 over time. Graph represents ±SEM; *n* = 12 leaf discs. Experiment is representative for two independent experiments with similar results. **g** Flg22-induced activation of MAPK in the indicated genotypes and time points. MAPK activation is revealed with anti-pERK antibodies. For control, FLS2 abundance and Coomassie brilliant blue (CBB) staining is shown. The experiment was repeated twice with similar results. **h** Infection analysis of the *net4ab-c2* crispr double mutants compared with wild type Col-0. Plants were surface inoculated with *P. syringae* pv. *tomato* (*Pto*) DC3000 wild type bacteria (OD₆₀₀ = 0.02), a strain defective in coronatine production (cor-) (OD₆₀₀ = 0.2), and a strain defective in Type-3-secretion of effectors (*Hrc-*) (OD₆₀₀ = 0.2). *In planta* bacterial growth was determined as colony forming units (cfu) at 3 dpi. Bar graphs represent mean values ± SEM of *n* = 8; *p* ≤ 0.01 (**). Experiments are representative for at least two independent experiments with similar results.

immunoprecipitates analysed by mass-spectrometry (Supplementary Table 2). The protein sequences of RABG3 members are very similar, which may account for the ability of NET4 proteins to interact with multiple isoforms. The relatively large number of branches within the RabG class in Arabidopsis may reflect the diversity of vacuoles and associated trafficking that have evolved in higher plants[26,29].

RABG3 family proteins are Rab7 GTPases, which cycle in an active, GTP-bound state and an inactive, GDP-bound state, which are determinants of their subcellular localization and likely interaction partners[30]. We therefore tested the interaction of NET4A and NET4B with both constitutive active (CA) and GDP-locked (TN) dominant negative (DN) variants of RABG3a and RABG3f. Only wild type and active, GTP-bound RABG3a and RABG3f interacted with NET4A and NET4B (Fig. 4a). We then addressed whether the association of NET4 proteins is specific to the RABG proteins or whether this interaction occurs more broadly across the Arabidopsis Rab GTPase families. Using RABD2a, RABA5c and RABF2a as baits, we identified no interaction with NET4B in Y2H (Fig. 4b), and similarly NET4B was not co-immunoprecipitated from Arabidopsis microsomes expressing YFP-RABA2a or YFP-RABA5c (Supplementary Table 2).

NET4 proteins contain a novel RABG3 specific binding motif

The C-terminus of NET4B contains a conserved domain with an invariable "IRQ" sequence, thus referred to as the IRQ domain (Fig. 4c, d). C-terminal deletion including the IRQ domain abolished the interaction of NET4B with CA-RABG3a (Fig. 4d, e). To define the minimal domain of the NET4B C-terminus that is required for the interaction with RABG3a, we tested a series of truncated IRQ domains with and without the C-terminus as Y2H baits against CA-RABG3a (Fig. 4d, f). This experiment identified residues 464–511 (47aa) of NET4B as the RABG3 binding domain, a novel RABG3-specific binding motif previously unknown in plants. We suggest that NET4 proteins associate to the tonoplast, because of their interaction with GTP-bound RABG3 GTPases through the IRQ domain. In agreement, we found that the interaction between RABG3a and NET4B was independent of its NAB domain, using a NET4B NAB deletion variant and the NAB domain alone as Y2H baits with CA-RABG3a as the prey (Fig. 4d, e).

RABG3b is required for proper flg22-induced stomatal closure

Having observed that NET4A and NET4B mediate stomatal closure to flg22, we determined the guard cell expression levels of all RABG3 family proteins by qRT-PCR. Although RABG3B, RABG3F and RAGB3E show high guard cell expression, the levels were not higher than those in mesophyll cells (Fig. 5a). Next, we obtained T-DNA insertional lines for all *RABG3* genes and screened the mutants for stomatal responses. Consistent with previous findings[31], stomata from *rabg3b* mutants did

not close in response to flg22 (Fig. 5b). This phenotype of stomatal closure was specific to RABG3b as none of the other tested *rabg3* mutants, including a *rab2g* mutant, showed altered closure of stomata to both flg22 and ABA (Fig. 5b). Phylogenetic analysis of the RabG3-subclass places the isoforms into two major branches, one containing RabG3c, RABG3d, RabG3e and RabG3f and a second contain RabG3a and b[32,33]. This structural distinction may in part explain why of those RABG proteins highly expressed in guard cells only *rabg3b* exhibits altered stomatal closure.

To validate our observations, we developed complementation lines. Immunoblot analysis of constitutively expressed GFP-RABG3b in the *rabg3b* background revealed signals of full-length GFP-RABG3b fusion proteins and free GFP (Supplementary Fig. 3a). However, confocal microscopy revealed strong signals at tonoplast structures in pavement and guard cells (Supplementary Fig. 3b). This is consistent with the previously described localization of other RABG3 family members[26], including RABG3f (Fig. 1c), and suggests that the accumulation of free GFP in the immunoblot analysis could be due to the tissue disruption. Of relevance, GFP-RABG3b expression was functionally complementing the impaired flg22-induced stomatal closure in the *rabg3b* mutant (Supplementary Fig. 3c, d). Furthermore, we developed lines expressing a DN variant of RABG3b. These plants exhibited impaired stomatal closure to flg22 treatment (Supplementary Fig. 3d), which is consistent with inactive, GDP-locked RabG3s showing no interaction with NET4A and NET4B (Fig. 4a).

We next evaluated the stomatal response to flg22 at two different time points and testing another PTI response pathway, with a second elicitor, fungal chitin. We detected that the *rabg3b* and *net4* mutants showed wild type-like stomatal closure after 1 h flg22 and chitin treatments but after 2 h, mutant stomata were open, while wild type stomata were closed (Fig. 5c, d, Supplementary Fig. 3e). This suggests a role for RabG3b and NET4 proteins in the robust closure of stomata upon elicitation, that is, inhibiting the reversibility of stomatal closure.

In agreement with wild type-like stomatal closure 1 h after elicitation, *rabg3b* was not generally immune-compromised, such as exhibiting wild type-like flg22-induced ROS production and MAPK activation (Fig. 5e, f), and did not show obvious defects on plant growth and development (Supplementary Fig. 3f). This is consistent with previous findings, reporting the requirement of *rabg3* higher order mutants to observe more macroscopic phenotypes[26].

Focussing on RABG3b, we performed co-immunoprecipitation analysis to investigate its association with NET4 proteins. Co-expression of NET4A-GFP and RFP-RABG3b in *N. benthamiana* showed an association of NET4A with wild type RABG3b as well as with CA-RABG3b but not DN-RABG3b (Fig. 6a). Additional Y2H screening using CA-RABG3b as a bait identified NET4A as the most prominent
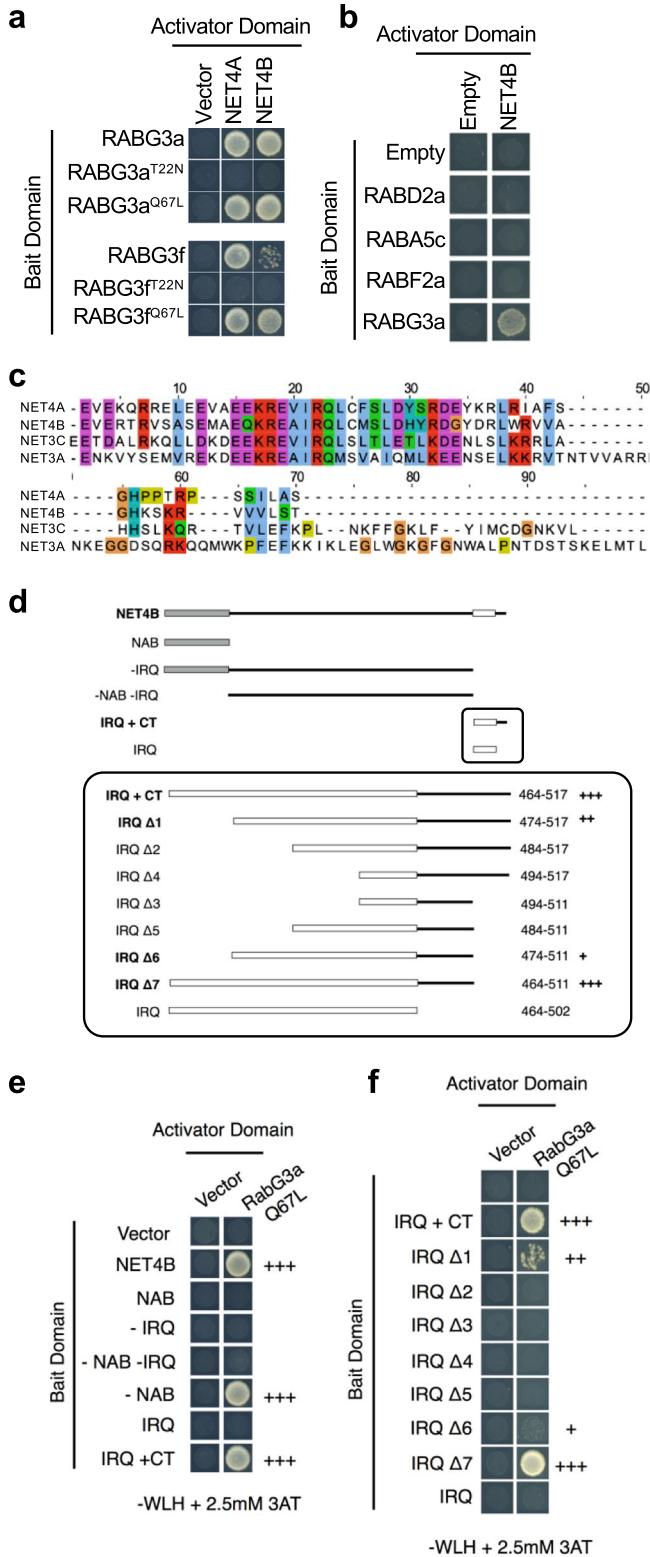
localising predominantly to the cytosol. It is therefore likely that NET4 family proteins may be regulated by active GTP-bound RabG3B at the vacuole (Supplementary Fig. 4).

To substantiate this claim, we aimed to examine whether the co-localization of NET4B and RabG3b was dependent on the IRQ domain of NET4B. We co-expressed NET4B-GFP wild type and the IRQ deletion variant with RFP-RABG3b and, as a tonoplast marker, mTAGBFP2-VAM3 in *N. benthamiana* leaves. Because the tonoplast membrane is very close to the plasma membrane in epidermal cells, observations of NET4-RabG3b co-localization is difficult. However, a fortuitous effect of this co-expression is the appearance of invaginations of the tonoplast membrane in some cells (Fig. 6b). This enabled us to monitor the ability of RabG3b to recruit NET4A to the tonoplast: (i) in the absence of RFP-RabG3b, NET4B-GFP signals were not detected at the mTAGBFP2-VAM3-positive tonoplast invaginations; (ii) upon RFP-RabG3b co-expression, NET4B-GFP was observed at the mTAGBFP2-VAM3-positive tonoplast invaginations and showed co-localization with RFP-RabG3b; (iii) this recruitment and co-localization was not observed when NET4B$^{\Delta IRQ}$-GFP was co-expressed with RFP-RabG3b and BFP-VAMP3 (Fig. 6b, c). In agreement with our Y2H findings (Fig. 4f), these observations demonstrate *in planta* that the IRQ domain of NET4 is required for the association of NET4 and RABG3 proteins and NET4 tonoplast localization.

NET4 proteins and RABG3 appear not to be involved in guard cell vacuole trafficking

Previous work demonstrated that RABG3 family members, together with RAB5 GTPases, mediate cargo trafficking to protein storage vacuoles[26]. Signalling-active, flg22-bound FLS2 is degraded involving endocytosis and trafficking along RAB5 GTPase-positive endosomal compartments destined for lytic vacuoles[34–36]. However, in FLS2 immunoblots we observed wild type-like flg22-reduced FLS2 abundance in *net4a* mutants (Fig. 3g), suggesting its normal degradation and endocytosis[35,37].

RABG3b has been previously implemented in the regulation of autophagy related to pathogen-triggered and developmental cell death[38,39]. Also, autophagy has been linked to steady-state abundance of FLS2 and with stomatal movements[40,41]. Thus, we decided to test autophagic flux in *net4ab* double mutant and *rabg3b* upon flg22 treatment. Autophagic flux is defined as the rate of delivery of autophagic substrates to the vacuole and used as a measure to assess autophagy in different mutant backgrounds[42]. We measured protein levels of (i) ATG8, the core autophagy protein that marks autophagosomes[43], (ii) NBR1, a well-established autophagy substrate[44], and (iii) catalase, a peroxisomal protein, since a recent study has shown that stomatal autophagy is crucial for peroxisome recycling[41]. To assess vacuolar delivery, we treated cells with Concanamycin A, which inhibits vacuolar ATPase and leads to the stabilization of autophagic substrates[44]. As a control, we used the *atg5* mutant, since in this mutant autophagic degradation is blocked[45]. Our immunoblot analysis in wild type seedlings revealed a strong flg22-dependent autophagy induction 2 hrs after treatment and

interactor (Supplementary Table 3). This agrees with our results on NET4 protein interaction with RABG3a and RABG3f (Fig. 4a), and further supports that NET4 proteins could represent effectors of RABG3 family members. Consistent with this, we confirmed that NET4 family proteins can interact with GTP-bound RabG3B at the tonoplast. In stable Arabidopsis transgenic lines co-expressing NET4A-GFP and RFP-RABG3b isoforms, we observed co-localisation of NET4A-GFP with RFP-RabG3B^{WT} and RFP-RabG3B^{CA} at the tonoplast. RFP-RabG3B^{DN} did not clearly co-localise with NET4A-GFP at the tonoplast, instead
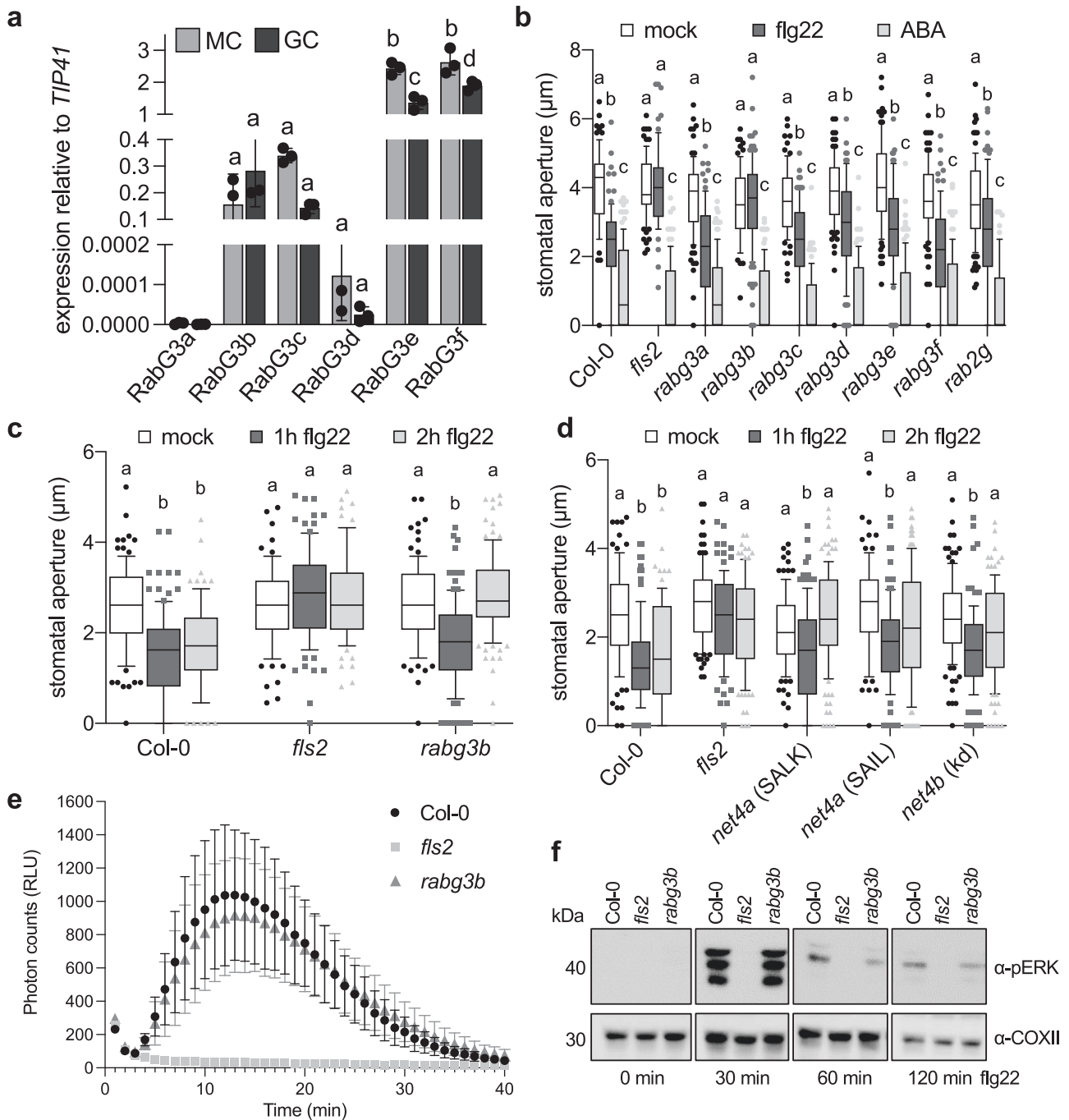
Fig. 5 | *rabg3b* mutants are impaired in robust flg22-induced stomatal closure. a Transcript levels of *RABG3* family members were quantified in guard cells (GC)-enriched samples or mesophyll cells (MC), respectively, relative to *TIP41*. Bars represent mean values ± SEM of 3 biological replicates (ANOVA with Bonferroni's Multiple Comparison Test). **b** Stomatal aperture measurements in *rabg3* and *rabg2* mutants, Col-0 and *fls2*. Apertures measured 2 h after treatment with 20 μM flg22 or 10 μM ABA. Box plots of the values are shown with whiskers from the 5th to 95th percentiles, the line in the box shows the median (Col-0 (mock) n = 76 stomata, Col-0 (flg22) n = 86, Col-0 (ABA) n = 105, *fls2* (mock) n = 82, *fls2* (flg22) n = 69, *fls2* (ABA) n = 105, *rabg3a* (mock) n = 91, *rabg3a* (flg22) n = 104, *rabg3a* (ABA) n = 117, *rabg3b* (mock) n = 79, *rabg3b* (flg22) n = 101, *rabg3b* (ABA) n = 99, *rabg3c* (mock) n = 77, *rabg3c* (flg22) n = 91, *rabg3c* (ABA) n = 99, *rabg3d* (mock) n = 91, *rabg3d* (flg22) n = 84, *rabg3d* (ABA) n = 99, *rabg3e* (mock) n = 91, *rabg3e* (flg22) n = 80, *rabg3e* (ABA) n = 99, *rabg3f* (mock) n = 91, *rabg3f* (flg22) n = 83, *rabg3f* (ABA) n = 99, *rab2g* (mock) n = 105, *rab2g* (flg22) n = 105, *rab2g* (ABA) n = 99 stomata). Different letters indicate significantly different values at p < 0.0001 (2-way ANOVA, multiple comparisons). The experiment was repeated twice with similar results. **c**, **d** Stomatal apertures measured in the indicated genotypes 1 and 2 h after treatment with 20 μM

flg22. Box plots of the values are shown with whiskers from the 5th to 95th percentiles, the line in the box shows the median (**c**: Col-0 (mock) n = 106 stomata, Col-0 (flg22 1 h) n = 110, Col-0 (flg22 2 h) n = 114, *fls2* (mock) n = 78, *fls2* (flg22 1 h) n = 92, *fls2* (flg22 2 h) n = 86, *rabg3b* (mock) n = 100, *rabg3b* (flg22 1 h) n = 112, *rabg3b* (flg22 2 h) n = 116 stomata); (**d**: Col-0 (mock) n = 100 stomata, Col-0 (flg22 1 h) n = 116, Col-0 (flg22 2 h) n = 91, *fls2* (mock) n = 100, *fls2* (flg22 1 h) n = 110, *fls2* (flg22 2 h) n = 104, *net4a* SALK (mock) n = 122, *net4a* SALK (flg22 1 h) n = 125, *net4a* SALK (flg22 2 h) n = 125, *net4a* SAIL (mock) n = 99, *net4a* SAIL (flg22 1 h) n = 102, *net4a* SAIL (flg22 2 h) n = 125, *net4b* kd (mock) n = 113, *net4b* kd (flg22 1 h) n = 99, *net4b* kd (flg22 2 h) n = 110 stomata). Different letters indicate significantly different values at p < 0.0001 (2-way ANOVA, multiple comparisons). The experiment was repeated twice with similar results. **e** ROS production measured as relative luminescence units (RLU) in the indicated genotypes treated with 100 nM flg22 over time. Graph represents ±SEM; n = 3 leaf discs. The experiment was repeated twice with similar results **f** Flg22-induced activation of MAPK in the indicated genotypes and time points. MAPK activation is revealed with anti-pERK antibodies. For loading control, COXII abundance is shown. The experiment was repeated twice with similar results.
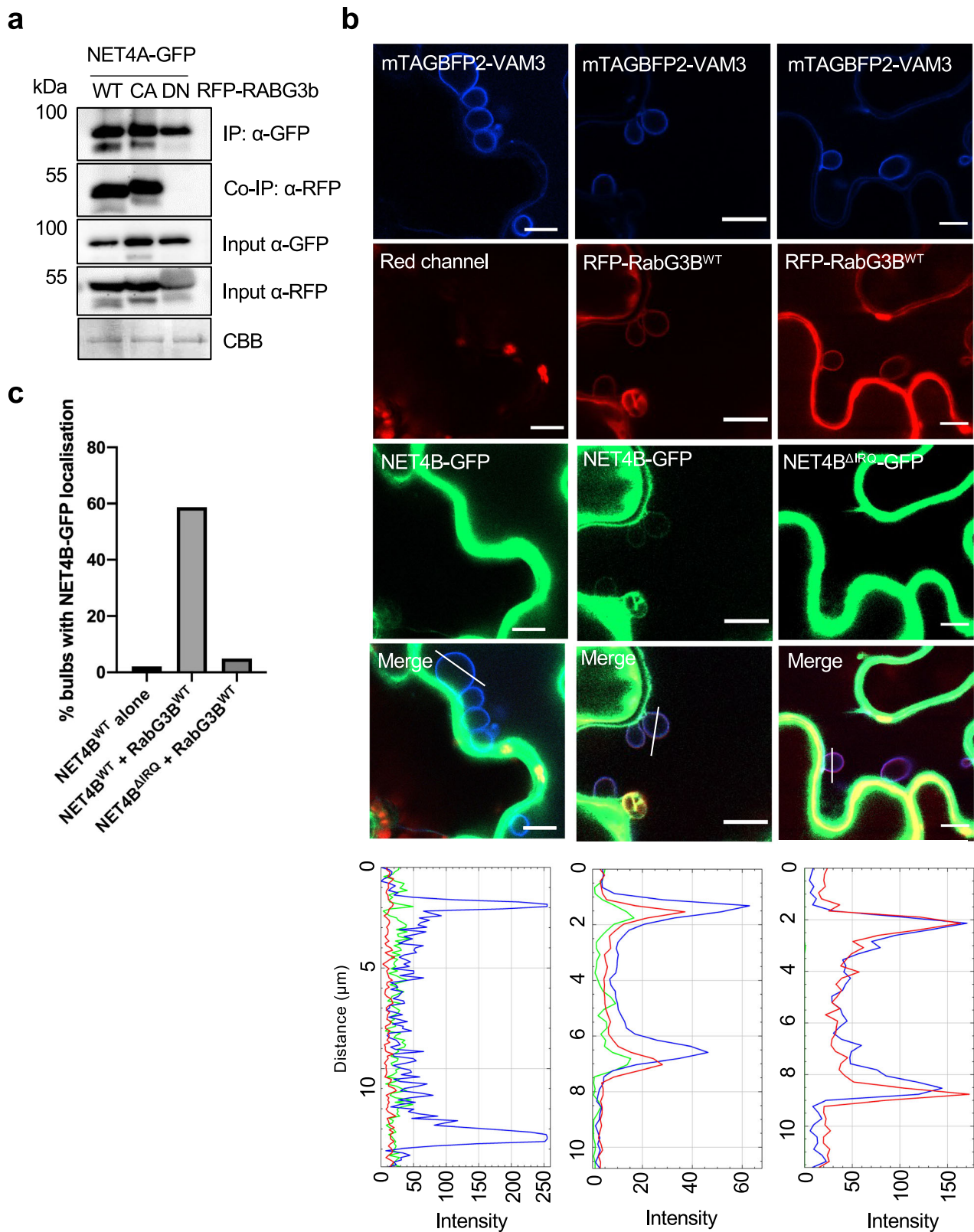
recovery (Supplementary Fig. 5a–c). Autophagic flux experiments using these conditions showed no significant difference between wild type, *net4ab* and *rabg3b* mutants (Supplementary Fig. 5d). Thus, despite we cannot exclude guard cell specific roles, as we analysed whole leaves and seedlings, we did not find major effects related to FLS2 trafficking and autophagic flux in *net4* and *rabg3b* mutants.

Vacuole morphology appears unaltered in *net4* and *rabg3b*

A subcellular output of stomatal closure is the change in vacuole morphology[12], and recently it was shown that NET4 proteins modulate the compactness of vacuoles[11]. Moreover, inhibition of RABG3 function in higher order mutants and by expression of a DN-RABG3f variant resulted in enlarged late endosomes and fragmented vacuoles[26,46]. To observe vacuole morphology in guard cells, we first used MDY-64 to

Fig. 6 | The RabGTPase activation status and the NET4 IRQ domain are determinants of the NET4-RabG3b association and localization. a Co-immunoprecipitation (Co-IP) assay of NET4A-GFP with wild type (WT), constitutive active (CA) and dominant-negative (DN) RFP-RABG3b. 1% of the input is shown as loading control. The experiment was repeated at least twice with similar results. **b** Confocal microscopy of *N. benthamiana* leaves transiently expressing RFP-RABG3b, NET4B-GFP or NET4B^{ΔIRQ}-GFP and the tonoplast marker mTAGBFP2-VAM3; scale bar = 10 μm. Images of the blue, red and green channels as well as merged channels are shown. Bulb-like mTAGBFP2-VAM3-positive tonoplast invaginations were observed in some transformed cells. Transections across mTAGBFP2-VAM3-positive tonoplast invaginations used for fluorescence intensity measurements are indicated by white lines. The histograms show mTAGBFP2-VAM3, RFP-RABG3b and NET4B-GFP or NET4B^{ΔIRQ}-GFP fluorescent intensities depicted by blue, red, and green lines, respectively. At least 30 tonoplast invaginations from at least 10 cells were imaged per series. The experiment was repeated twice independently with similar results, from across which representative images have been used. **c** Quantification of mTAGBFP2-VAM3-positive tonoplast invaginations with NET4B-GFP localisation. In the absence of RFP-RabG3b, NET4B-GFP signal was observed at 2% of tonoplast invaginations. When co-expressed with RFP-RabG3b, NET4B-GFP signal was observed at 58.7% of tonoplast invaginations. NET4B^{ΔIRQ}-GFP was observed at 4.9% of tonoplast invaginations when co-expressed with RFP-RabG3b.

stain the guard cell tonoplast in the *net4ab* double mutant, which was wild type-like (Supplementary Fig. 6a). Secondly, we developed transgenic lines expressing the tonoplast marker YFP-VAMP711 in the *rabg3b* background[47]. Confocal microscopy revealed no obvious effects in guard cell and pavement cell tonoplast morphology in *rabg3b* compared to wild type (Supplementary Fig. 6b). Similar observations were made with *rabg3b* mutants expressing GFP-RABG3f (Supplementary Fig. 6c). Flg22-stimulated wild type guard cells exhibited tonoplast patterns reminiscent of deflated vacuoles (Supplementary Fig. 6d). Guard cells of *rabg3b* showed tonoplast patterns of inflated vacuoles independent of flg22 treatment (Supplementary Fig. 6d).

We next used 2′, 7′-bis (2-Carboxyethyl)−5(6)-carboxyfluorescein (BCECF) as a luminar vacuole stain[48], revealing no difference in uptake between wild type and *rabg3b* guard cells and independent of the treatment conditions (Supplementary Fig. 6e). Using 3D image reconstruction and surface rendering we measured guard cell vacuole volumes[49,50]. Consistent with triggering stomatal closure, flg22-treated wild type guard cells showed a strong decrease in the vacuole volume and structures reminiscent of vacuole fragmentation or intra-vacuolar structure (Supplementary Fig. 6f, g)[12]. The volume of vacuoles in *net4ab* and *ragb3b* guard cells were not changed upon 2 hrs flg22 exposure, because in this condition stomata were open in these mutant backgrounds (Supplementary Fig. 6e, f). These data show a correlation between vacuole morphology and the open and closed status of stomata[12], which is also the case for open stomata in 2 hrs flg22-treated *net4* and *rabg3b* mutants.

### NET4A/B affects the dynamic reorganization of the actin cytoskeleton

It was previously shown that PTI signalling changes the guard cell actin cytoskeleton organization[25,28]. Since NET4 proteins interact with F-actin and co-localize with actin filaments (Fig. 1, Supplementary Fig. 1), we next investigated the effect of NET4A/B on cytoskeletal organization. We developed transgenic Col-0 and *net4ab-c2* double mutant plants expressing the actin marker Lifeact-mNeon and applied quantitative image analysis of actin filament organization in guard cells from these lines. We measured the mean angular difference and parallelness of actin filaments[28], which were similar in guard cells of open stomata from Col-0 and *net4ab-c2* (Fig. 7a−c). Interestingly, guard cells from *net4ab-c2* mutants showed a lower value in the mean angular difference and a higher value in parallelness compared with Col-0 guard cells when treated with flg22 for 1 h (Fig. 7d−f). At 2 hrs flg22 treatment, the mean angular difference and parallelness of actin filaments was similar in Col-0 and *net4ab-c2* guard cells (Fig. 7g−i), despite the facts that Col-0 stomata were closed and *net4ab-c2* stomata were open (Supplementary Fig. 7). Over the time points of 1 and 2 hrs flg22 treatment, incremental changes occurred in Col-0 guard cells, showing the lowest value in mean angular difference and the highest value in parallelness at 2 hrs (Fig. 7a, d, g). This suggests that the actin cytoskeleton changes from a radial to a more longitudinal organization, a pattern correlating with stomatal closure and consistent with closed apertures in flg22-treated Col-0 (Supplementary Fig. 7). By contrast,

the mean angular difference was lowest and the parallelness was highest at the 1 h time point in *net4ab-c2* guard cells, which then again increased and decreased, respectively, at 2 h flg22 treatment (Fig. 7b, e, h). These results reveal that the *net4ab-c2* mutants are compromised in guard cell actin cytoskeletal remodelling with an enhanced actin rearrangement, showing a stronger response at 1 h and an earlier shift in the recovery at 2 h flg22 treatment. This demonstrates that actin cytoskeletal organization by NET4 proteins is required for normal stomatal closure to flg22, possibly inhibiting the reversibility of the closure process. Taken together, these data suggest that actin remodelling upon elicitation contributes significantly to stomatal closure but is not mutually exclusive from other events regulating compact vacuole morphologies, e.g. ion flux-driven deflation (Supplementary Fig. 6).

Discussion

Using molecular and cell biology approaches, we provide evidence for a molecular link between actin cytoskeletal organization and the vacuole morphologies underlying guard cell shape changes. We show that the two NET4 proteins have the potential to localize simultaneously to actin filaments and the vacuole tonoplast, mediated by two distinct domains: the family-characteristic NAB domain is involved in F-actin binding whereas the newly identified specific IRQ domain confers the direct interaction with RABG3 GTPases (Figs. 4, 6, Supplementary Fig. 1). This is compatible with the possibility that the tonoplast localization of NET4A and NET4B occurs through RABG3 GTPases. Indeed, proper NET4 localization depends on the presence of the IRQ domain and RABG3b co-expression (Fig. 6b). We noted that the interaction between the NET4 proteins and the RABG3 GTPases perfectly correlated with the tonoplast-localized and active, GTP-bound state of the Rab7 GTPases (Figs. 4, 6, Supplementary Fig. 4)[30]. A simple possibility to explain this correlation is to postulate that NET4A and NET4B are effectors of RABG3 GTPases. Consistent with this hypothesis is that *net4* and *rabg3b* mutants have similar phenotypes, exhibiting impaired stomatal closure after 2 hrs PAMP treatment (Fig. 5). Thus, the tonoplast localization of the NET4 proteins can be linked to RABG3 GTPases, which may aid actin-tonoplast tethering in an activation-dependent manner.

Remodelling of the actin cytoskeletal organization is increasingly acknowledged as a critical function of plant immunity including stomatal movements[51]. Moreover, patterns of actin cytoskeletal organization have been associated with different vacuole morphologies in plant growth[10,11]. In this study, we identify that the NET4 proteins are involved in guard cell actin reorganization that is triggered by FLS2 signalling. We found that open stomata of *net4* and *rabg3b* mutants after 2 hrs flg22 treatment exhibited (i) more longitudinal arrayed actin filaments (Fig. 7), which represents an actin organization normally correlating with closed stomata and (ii) showed vacuole morphologies consistent with inflation (Supplementary Fig. 6), which correlates with open stomata. Furthermore, we showed that (iii) RabG3b recruited NET4B to tonoplast membranes via IRQ domain-mediated interaction (Fig. 6); and that (iv) *net4* and *rabg3b* mutants exhibited closed stomata after 1 h flg22 treatment but open stomata at
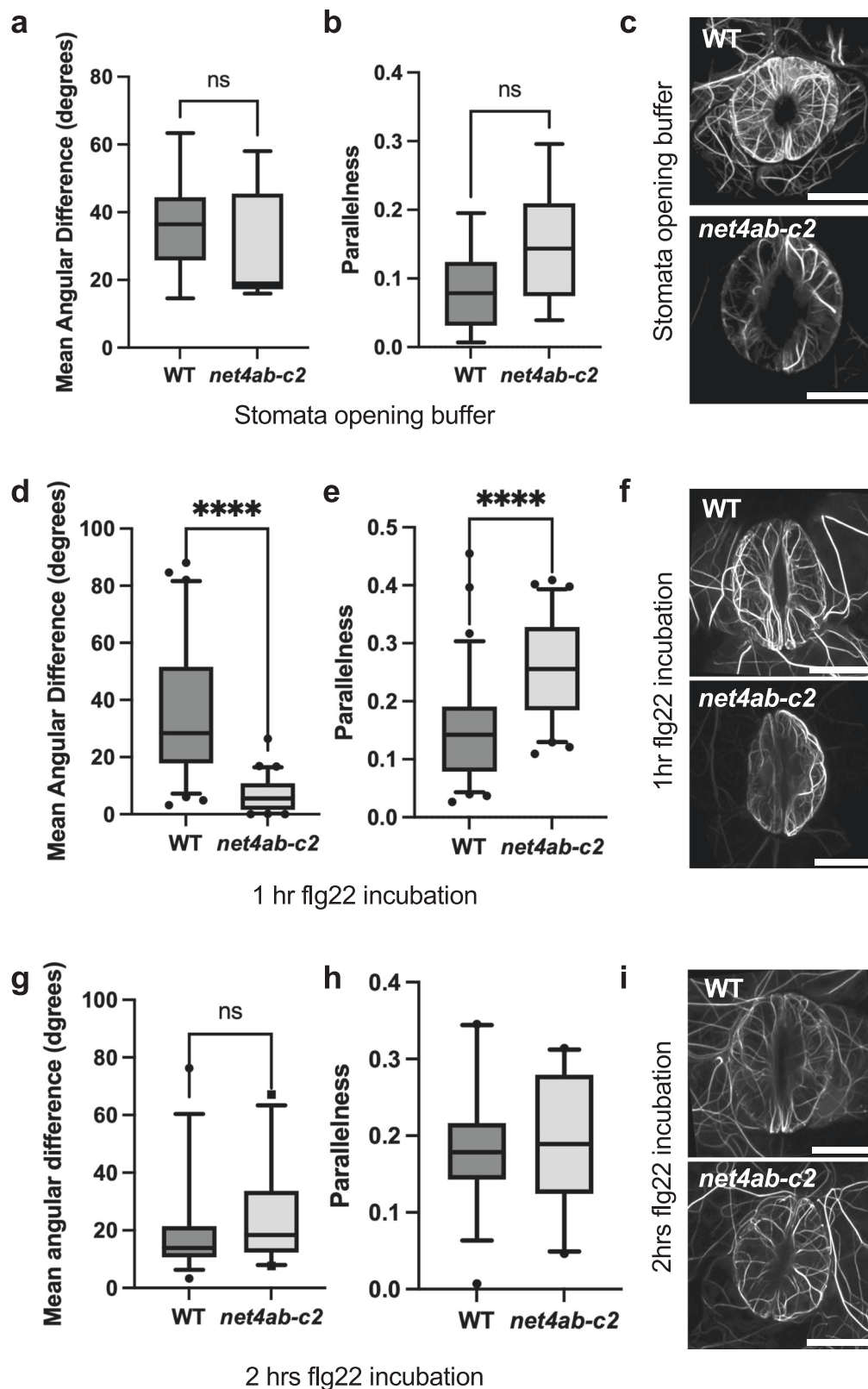
2 h flg22 treatment (Fig. 5). These results are compatible with a model (Supplementary Fig. 8), that NET4-RABG3b actin-tonoplast tethering may facilitate to maintain compact vacuole morphologies correlating with deflation, a process driven by transient changes in ion and water fluxes[18], and thus may constrain the reversing of closed to open stomata. In mutant guard cells of the NET4-RabG3b couple, FLS2 signalling would result in osmotic change-driven deflation and actin reorganization, triggering initial stomatal closure. Disconnection of the two processes, actin reorganization and vacuole morphology changes, would allow for too early re-inflation of the vacuole and re-opening of stomata, thus impaired robust PAMP-induced stomatal closure. This is consistent with transient signatures of ion fluxes downstream of FLS2 signalling, NET4A localizing to constricted vacuolar membranes and NET4A modulating vacuole compactness in

Fig. 7 | Guard cell actin dynamics are altered in *net4* mutants.
a, b, d, e, g, h Quantification of actin cytoskeletal patterns of Lifeact-mNeonGreen-expressing Col-0 WT and *net4ab-c2* plants in guard cells. ImageJ analysis using the LPIXEL Inc LPX plugin set. **a, b** Mean angular difference (**a**) and parallelness (**b**) of the actin cytoskeleton in untreated guard cells. **d, e** Mean angular difference (**d**) and parallelness (**f**) of the actin cytoskeleton in guard cells treated for 1 h with flg22. **g, h** Mean angular difference (**g**) and parallelness (**h**) of the actin cytoskeleton in guard cells treated for 2 h with flg22. Box plots of the values are shown with whiskers from the 5th to 95th percentiles, the line in the box shows the median; 1 h

flg22 treatment: WT Col-0 $n = 73$, *net4ab-c2* $n = 64$ guard cells, $p < 0.0001$ Mann Whitney *t*-test; 2 h flg22 treatment: WT Col-0 $n = 38$, *net4ab-c2* $n = 23$ guard cells, $p = 0.0777$ ns Mann Whitney *t*-test; Stomata opening buffer: WT Col-0 $n = 10$, *net4ab-c2* $n = 7$ guard cells, - angle $p = 0.3638$, parallelness $p = 0.1088$ ns Mann Whitney *t*-test. **c, f, i** Representative super-resolution Airyscan confocal images of Lifeact-mNeonGreen-positive actin filaments in Col-0 WT and *net4ab-c2* untreated and treated for 1 and 2 hrs with flg22, respectively. Scale bars = 10 μm. The experiments were repeated at least thrice with similar results.

meristematic cells[11]. Notably, our model would accommodate for the need of multiple cycles of remodelling/aligning, in that the activity of RABG3b may release the NET4 tethers from the interaction, allowing for reloading of the GTPase with GTP and further cycles. The signal-specificity and responsiveness of the *net4* mutant stomatal phenotype also fulfils the requirement for reversibility of the molecular and thus subcellular interactions in our model.

Activation of PRRs leads to the closure of stomata, through short signalling cascades regulating ion channels and ROS production from RBOHD[18,22,52]. Active PRRs also induce actin cytoskeletal changes, involving the calcium-dependent protein kinase CPK3 and MPK3/6, downstream of FLS2, and their substrates ADF4 and VLN3[25,53,54]. Future research will answer whether RABG3b could be a substrate of FLS2 signalling and upon phosphorylation interact with a GTP exchange factor, similar to human RAB7 tyrosine-phosphorylation by the Src kinase[55]. If so, this signalling-dependence of additionally available GTP-bound, active RABG3b would further promote the process of NET4-driven vacuolar tethering of actin filaments potentially helping the inhibition of reopening stomatal pores. Molecular links between actin-membrane interactions and signalling events have been identified previously between NET2A PRK4 and 5[5], suggesting that short signalling cascades could regulate actin-membrane contact sites and therefore the underlying actin organisation.

The physiological significance of PAMP-induced stomatal closure and its molecular mechanisms are increasingly understood[18]. Infectious pathogens actively interfere with the signalling events leading to pore closure: for example, *Pto* DC3000 produces coronatine, which activates reopening of stomata, and delivers HopM1 into plant cells, which can inhibit stomatal closure[18]. This might explain our observation that *net4ab-c2* double mutants showed wild type-like bacterial growth upon infection with virulent *Pto* DC3000 and the disarmed Pto DC3000 cor- strain but showed increased bacterial growth of the non-virulent *Pto* DC3000 *Hrc*- strain (Fig. 3h). Pathogens are also known to subvert host subcellular pathways, for example by targeting the actin cytoskeleton and Rab GTPases[56–59], altogether highlighting a crucial role of actin- and Rab-dependent processes in immunity. Whether NET4 proteins and RABG3b are pathogen effector targets remains to be shown.

We note that *net4* and *rabg3b* mutants have no obvious global developmental and infection-related phenotypes. Also, the impaired stomatal closure is specific to PAMPs and no general phenotype. This raises questions whether other members of the NET family could have partial redundant functions to NET4A and NET4B, for example NET3A/C, also having IRQ domains, and further higher order mutants combining *net4a/b* and *net3a/c* might be needed (Fig. 4c). Roles for NET4 proteins beyond the guard cell may require distinct RabG isoforms found in those tissues and here, the additional IRQ domain containing NET3A/C may partially perform NET4 functions. Of note, guard cell immune responses appear to involve components not essential for other immune responses including the calcium-permeable channel OSCA1.3, which is also not required for ABA-induced stomatal closure[60].

Taken together, in this study we provide a molecular-subcellular framework of PAMP-induced stomatal closure through NET4-RABG3b. Our findings suggests that the inhibition of reversing closed stomatal

pores is directed by the coordination of actin cytoskeletal and vacuolar remodelling and this is mediated by NET4-RabG3b actin-tonoplast tethering. Our findings also raise the possibility that RABG3b, which has already been implicated in membrane fusion at the vacuole[26], may have additional functions in linking the tonoplast with actin rearrangements.

Methods

Plant materials and growth conditions

For assays with adult Arabidopsis plants, plants were grown on soil for 5 weeks in controlled environment rooms under short day conditions (10 h light at 22 °C and 14 h dark at 20 °C, 65% humidity). Arabidopsis seedlings were grown under sterile conditions in 24-well plates containing liquid medium (Murashige and Skoog Basal Medium (including vitamins), Duchefa, Haarlem, The Netherlands) for 14 d at 22 °C in a 16 h photoperiod. For live cell microscopy, transformed and crossed Arabidopsis lines were grown in the same conditions as described above. For *Nicotiana benthamiana* leaf transient transformation assays, *N. benthamiana* plants were grown on soil in controlled environment rooms under a 16 h photoperiod at 25 °C and 8 h darkness at 21 °C.

fls2 mutants were obtained[61]. Homozygous T-DNA insertion lines *rabg3a-f, rabg2, net4a* and *net4b* were obtained from SAIL and SALK populations (Supplementary Table 4). To constitutively express VAMP711-YFP in *rabg3b* mutant background, the pNIGEL07 vector carrying VAMP711-YFP fusion protein under control of the UBI10 promoter was transformed into SALK_004938[62]. Stable transgenic GFP-RABG3b lines were generated by cloning the genomic coding sequence of *RABG3b* either into the pUBN-GFP-Dest vector for constitutive expression or in fusion with 1180 bp of its native promoter into pCAMBIA1390 and Agrobacterium-mediated stable transformation into the *rabg3b* mutant background[62,63]. Stable transgenic *pUb-i10*::RFP-RabG3b, *pUbi10*::RFP-CA-RabG3b, and *pUbi10*::RFP-DN-RabG3b were generated by PCR cloning the genomic coding sequence into the pUBN-RFP-Dest vector, introducing the respective mutations using corresponding primers, and Agrobacterium-mediated stable transformation into *A. thaliana* Col-0. The mutations were confirmed by sequencing. The FLS2-GFP construct was obtained[61]. All constructs were confirmed by sequencing. *atg5-1* (AT5G17290, ATG5, SAIL_129B07) mutants were obtained[45].

Stable transgenic *pNET4A*::NET4A-GFP lines were generated by cloning 2 kb of the promoter and genomic sequence of *NET4A* into pMDC107 and Agrobacterium-mediated stable transformation into Arabidopsis Col-0. *pNET4A*::NET4A-GFP lines were crossed with *pUb-i10*::mCherry-RabG3f[50] for generating stable transgenic co-expressing lines. To create *NET4A* or *NET4B* promoter GUS reporter lines, 2 kb promoter sequence of each gene was cloned in pBI101G and introduced into Col-0 by Agrobacterium-mediated stable transformation. Double *net4a/net4b* mutants were created by CRISPR/Cas9 gene editing. The *net4a.1* T-DNA insertion line was transformed with a vector driving EC1.2en:EC1.1 controlled expression of 3 × FLAG-NLS-zCas9-NLS, which carried two *NET4B* gRNA modules. The nature of the mutation in the *net4ab-c2* CRISPR-Cas9 double mutant is a t insertion in *NET4B*, which gives a frameshift in the latter part of the NAB domain, leading within two codons to a STOP codon. To analyse CRISPR/Cas9

generated genomic editing events, fragments surrounding the target sites were amplified by PCR using gene-specific primers N4B_F and N4B_R and sequenced using a nested primer (N4B_Fn1).

Actin marker lines expressing Lifeact-mNeonGreen were generated through Agrobacterium-mediated stable transformation of Col-0 and *net4ab-c2* CRISPR-Cas9 double mutants. The Lifeact-mNeonGreen DNA coding sequence was synthesised (Integrated DNA Technologies) including gateway arms for downstream cloning. The final destination clone used to transform *net4ab* CRISPR-Cas9 double mutant consisted of this sequence recombined into pH7WG2.

Transient transformation of *N. benthamiana*
For transient expression of proteins in *N. benthamiana*, constructs were transformed into *Agrobacterium tumefaciens* strain GV3101 and syringe infiltrated into young leaves. Cultures were infiltrated at OD600 between 0.1 and 0.4 and leaves imaged 2–3 days post infiltration. For analysis of NET4B-GFP, RFP-RabG3b and mTAGBFP2-VAM3 in *N benthamiana*, combinations of NET4B-GFP and RFP-RabG3b were infiltrated initially, and mTAGBFP2-VAM3 was subsequently infiltrated into the same leaf tissue 3 days later. To transiently express NET4A and NET4B, their coding sequences were recombined into pCaMV35S driven binary GFP fusion destination vectors: pMDC43 (N-terminal GFP), pMDC83 (C- terminal GFP), pH7WGR2 (N-terminal mRFP). GFP-NET4BΔIRQ + CT was generated by cloning NET4B coding sequence residues 1-464 into pMDC43. mCherry-FABD2 construct encodes the C-terminal half of AtFIMBRIN1, which encompasses the second actin-binding domain of the protein[64] fused to an N-terminal mCherry fluorescent tag. Lifeact-RFP consists of the 17 aa actin binding domain of Lifeact cloned into pH7RGW2 to produce an actin marker with a C-terminal red fluorescent protein tag[5].

The mTAGBFP2-VAM3 construct was expressed using the destination vector, pMDC43-mTAGBFP2, which drives the expression of N-terminal mTAGBFP2-tagged fusion proteins under the *CaMV*35S promoter. To generate pMDC43-mTAGBFP2, the mTAGBFP2 coding sequence was PCR-amplified using the primers mTAGBFP2-F and mTAGBFP2-R to generate a fragment with 5' Acc65i and 3' AscI restriction sites. The resulting 5'-Acc65i-mTAGBFP2-AscI-3' fragment was cloned into the Acc65i/AscI restriction sites of pMDC43 using restriction subcloning. To label tonoplast membranes, the VAMP3 coding sequence was PCR amplified from Arabidopsis cDNA using the primers VAMP3-F and VAMO3-R. pMDC43-mTAGBFP2 was linearised using SacI/BsrGI restriction digestion and the VAM3 coding sequence was inserted into the linearised vector using hot fusion cloning[65].

Stomatal closure assay
Leaf discs were harvested from at least 4 individual adult Arabidopsis plants per genotype and treatment using a biopsy puncher (4 mm width) and incubated for 3 h in the light in stomata assay buffer (10 mM 2-(N-morpholino)-ethanesulfonic acid (MES) pH 6.1, 50 mm KCl, 10 μm CaCl2, 0.01% Tween). After a subsequent 2 h treatment with 10 μM ABA, 20 μM flg22 or 100 mg/ml chitin (in stomata assay buffer in the light), stomata in the lower leaf epidermis were imaged using a bright field microscope DM-R (Leica, http://www.leica.com) at 40× magnification. Three images per leaf discs were captured and aperture sizes of the stomata within the field of imaging were measured using ImageJ[66].

ROS assay
ROS assays were performed as reported[67]. Briefly, leaf discs were harvested with a biopsy puncher (4 mm width), placed in a 96-well plate, with a minimum of 12 leaf discs per genotype per assay, and incubated overnight in 200 μl of water in the dark. The water was then replaced with 100 μl of a luminol (0.4 mM)/peroxidase (20 μg/ml−1 horseradish peroxidase, Sigma, www.sigmaaldrich.com) solution with or without (mock) 100 nM flg22. A Photek camera system and software

were used to detect the luminescence over 45 min and 180 min. Quantification of luminescence are binned values from 60 s.

Bacterial infection assay
Bacteria were grown on King's B medium agar plates for 2 d at 28 C, cells were harvested and resuspended in 10 mM MgCl2 with 0.04% Silwet L-77. The leaves of 5-weeks-old Arabidopsis plants were sprayed from below and on top with *Pseudomonas syringae* pv. *tomato* (*Pto*) DC3000 or cor- (DC3118) or *Hrc*- at OD600 of 0.02 and 0.2 and 0,2 respectively. At 3 dpi, 4 pools of 4 leaf discs (6 mm width) each were harvested from at least 6 individual plants per genotype and grinded in 10 mM MgCl2 to extract the bacteria. To determine bacterial growth, dilution series of leaf extracts were plated in replicate on LB agar medium containing the appropriate antibiotics.

Gene expression analysis
Gene expression was studied in cDNA from whole seedlings, 15-days old vertically grown seedlings of the homozygous T-DNA insertion lines (*net4b.1, net4a.1 and net4b.1/net4a.1*), and in cDNA from enriched guard cell and mesophyll extracts (obtained from H. Kollist; University of Tartu, Estonia)[68]. Transcripts of the respective genes were quantified using real-time quantitative PCR with SYBR Green reagents and procedures (Applied Biosystems or SensiFAST SYBR DNA polymerase No-ROX Kit), and amplification was detected with the ABI PRISM 7700 Sequence Detection System or Rotor-gene Q PCR machine (Qiagen). For normalisation, the ΔCT method was used[69]. Reverse transcription-PCR was also used to analyse the disruption of the *NET4B* and *NET4A* transcripts in the homozygous *net4b.1*, *net4a.1* and *net4b.1/net4a.1* T-DNA insertion lines. RT-PCR and qPCR primers are summarised in Supplementary Table 5.

GUS expression analysis
Plant tissue was incubated in GUS staining solution (100 mM phosphate buffer, 10 mM EDTA pH8.0, 0.1% (v/v) Triton X-100, 0.5 mM potassium ferricyanide, 0.5 mM potassium ferrocyanide, 1 mM X-Gluc (5-bromo-4-chloro-3-indolyl-β-D-glucuronide, Melford). Samples were imaged using a Zeiss Axioskop, Leica DM2500, and a Leica MC165 FC microscope with a Photometrics Coolsnap cf camera (Openlab 3.1.1 software) or Leica DFC420C camera (LAS AF).

Yeast two hybrid one-on-one interaction assay
Full length NET4A, NET4B and RAB coding sequences, and truncation fragments were Gateway-cloned into pGBKT7 or pGAD bait and pray vectors. CA- and DN-RABG3 variants were generated by site directed mutagenesis with QuickChange Lightning II Site-Directed Mutagenesis Kit (Agilent Technologies) according to manufacturers' instructions. Bait and prey vectors (pGBKT7 and pGADT7) were transformed into the yeast strains AH109 and Y187, respectively. Single colonies of the bait and prey vector were mated on solid YPDA plates at room temperature for 24–48 h. As a negative control for auto-activation, above colonies were also mated with the respective empty vectors. Mated cells were selected by transfer onto to solid SD -WL dropout media. Diploid colonies were transferred onto selective SD dropout media −WLH + 2.5 mM 3AT and incubated at 30 °C for 5–7 days to test for potential interactions. As a positive control for yeast growth, diploid colonies were also grown on -WL SD plates. Yeast-two-hybrid screening using CA-RABG3b as a bait against a Arabidopsis prey cDNA library done by HYBRiGENiCS (https://www.hybrigenics-services.com/).

Protein biochemistry
For co-immunoprecipitation (co-IP) from Arabidopsis, seedlings were grown in 6-well plates containing liquid MS medium (1% sucrose) and for each time point and genotype, seedlings of one 6-well plate with 15–20 seedlings per well were pooled and transferred into a beaker containing 50 ml liquid MS medium. After 1 h of resting, flg22 (10 μM)

was added to all samples but mock treatment and vacuum infiltrated for 5 min. Seedlings were harvested at the indicated time points and flash frozen in liquid nitrogen and subjected to protein extraction. Mock treatment was harvested at 30 min after treatment. For co-IP from *Nicotiana benthamiana plants*, 5–6 weeks old plants were infiltrated with Agrobacteria strains (GV3101 pMP90, OD600 0.3) expressing the proteins of interest. After 3 days, 2 infiltrated leaves were detached and transferred into a beaker containing 150 ml H2O supplemented with 10 μM flg22 or not (mock), which was vacuum infiltrated for 3 min. Leaves were dried and flash frozen in liquid nitrogen. Tissue was grinded and transferred to centrifugation tubes. Total proteins were extracted using 1 ml of extraction buffer (50 mM Tris HCL pH 7.5, 50 mM NaCl, 10% glycerol, 2 mM EDTA, 2 mM DTT, 1% protease inhibitor cocktail (SIGMA), 1% PMSF, 1% phosphatase inhibitor cocktails 2 and 3 (SIGMA), 1% IGEPAL) per 1 ml grinded plant tissue. Samples were incubated in extraction buffer for 30 min rotating at 4 °C. Upon centrifugation (20 min, 20627 × g, 4 °C), supernatant was filtered with miracloth and BioRad column. A 100 μl aliquot of the supernatant was supplemented with 30 μL 6xSDS sample buffer and used as input protein sample. 10 μl GFP-Trap®_A beads (Chromotek; www.chromotek.com) were added to the residual supernatant and the immunoprecipitation incubated for 3 h rotating at 4 °C. Beads were collected upon centrifugation (1 min, 500 × g) and washed three times in wash buffer (50 mM Tris-HCl pH 7.1, 50 mM NaCl, 1% PMSF, 0.5% IGEPAL). After the final wash, the supernatant was completely removed and 60 μl 2× SDS sample buffer was added to the beads (IP). Before loading and running 25 μl of the samples on an SDS PAGE (10% SDS gel), they were boiled for 10 min at 95 °C. Proteins were transferred from the SDS gel onto a PVDF membrane through semi-dry western blotting. Membranes were incubated with the respective primary antibodies as indicated. After 3 washes with TBS-T, membranes were incubated with the respective secondary antibodies for 1.5 h. After washing the membranes in TBS-T, membranes were developed using SuperSignal™ West Femto Maximum Sensitivity Substrate (Thermo Fisher) and exposure to X-ray film (Fujifilm Super RX) for 2 min to 4 h, depending on the samples.

LC-MS/MS analysis and data analysis

Tandem affinity purification coupled to mass spectrometry (TAP-MS) of TAP-tagged NET4A was carried out as part of the AP-MS platform service provided by the Functional Interactomics group at the Centre for Plant Systems Biology VIB-Ghent. The NET4A ORF was transferred from pDONR207 into a GSrhIno tag vector by Gateway cloning to fuse with a double affinity tag, which consists of a protein G tag and a streptavidin-binding peptide separated by a very specific protease cleavage site. Arabidopsis cell suspension cultures were transformed, and *in planta* protein complexes were isolated using two sequential purification steps. In total four NET4A TAP samples were analyzed, each extracted and purified in the presence of a different detergent, DMM, digitonin, Triton-X-100 and C12E8. Eluted proteins were separated on SDS-PAGE with a short run and digested in-gel with Trypsin as described before[70]. The obtained peptide mixtures were introduced into an LC-MS/MS system, the Ultimate 3000 RSLC nano (Dionex, Amsterdam, The Netherlands) in-line and data analysis connected to an LTQ Orbitrap Velos (Thermo Fisher Scientific, Bremen, Germany). The sample mixture was loaded on a trapping column (made in-house, 100 μm internal diameter (I.D.) x 20 mm (length), 5 μm C18 Reprosil-HD beads, Dr. Maisch GmbH, Ammerbuch-Entringen, Germany). After back-flushing from the trapping column, the sample was loaded on a reverse-phase column (made in-house, 75 μm I.D. × 150 mm, 5 μm C18 Reprosil-HD beads, Dr. Maisch). Peptides were loaded with solvent A (0.1% trifluoroacetic acid, 2% acetonitrile), and separated with a 30 min linear gradient from 98% solvent A' (0.1% formic acid) to 55% solvent B' (0.1% formic acid and 80%

acetonitrile) at a flow rate of 300 nl/min, followed by a wash step reaching 97% solvent B'.

The mass spectrometer was operated in data-dependent mode, automatically switching between MS and MS/MS acquisition for the ten most abundant peaks in a given MS spectrum. In the LTQ-Orbitrap Velos, full scan MS spectra were acquired in the Orbitrap at a target value of 1E6 with a resolution of 60,000. The ten most intense ions were then isolated for CID fragmentation in the linear ion trap, with a dynamic exclusion of 40 s. Peptides were fragmented after filling the ion trap at a target value of 1E4 ion counts. The raw data was processed with Mascot. First, Mascot Generic Files were created using the Mascot Distiller software (version 2.4.3.1, Matrix Science, London, UK). Grouping of spectra was allowed with a maximum intermediate retention time of 30 s and a maximum intermediate scan count of 5 was used where possible. Grouping was done with 0.005 Da precursor tolerance. A peak list was only generated when the MS/MS spectrum contained more than 10 peaks. There was no de-isotoping and the relative signal-to-noise limit was set to 2. These peak lists were then searched with the Mascot search engine (version 2.4.1, Matrix Science) using the Mascot Daemon interface. Spectra were searched against the TAIRplus database[70] containing 35839 protein sequence entries. Fixed modification was set to carbamidomethylation of cysteine, and variable modifications were set to oxidation of methionine and methylation of aspartic acid and glutamic acid. Peptide mass tolerance was set to ±10 ppm (with Mascot's C13 option set to 1), and the fragment mass tolerance was set to ±0.5 Dalton (Da). The peptide charge was set to 2+ and 3+, and instrument setting was ESI-TRAP. The enzyme setting was trypsin allowing for one missed cleavage, and cleavage was allowed when arginine or lysine were followed by proline. Minimum peptide length was six. Peptide- and protein-level FDR were both set to 0.01. Proteins with at least two matched peptides of which at least one was unique, were retained. Background proteins were filtered out based on frequency of occurrence of the co-purified proteins in a large dataset containing 543 TAP experiments using 115 different baits classified into 62 unrelated bait groups[70]. Thereto, the identified protein lists were compared to the list of 760 nonspecific proteins as published[70] and only the specific binders were retained.

To test for RABG3 interactors in vivo, total *Arabidopsis* root microsomes were isolated from plants expressing YFP::RabG3f (Wave-5Y) 50, YFP::RABA2a 74, YFP::RABA5c 75 or no transgene. 20–30 surface-sterilised seeds were grown in 20 ml medium (0.3x Murashige and Skoog medium (Sigma, Poole, UK), 1% sucrose, 0.05% MES pH5.7) under 60 rpm shaking, 16 h days and 21 °C for 14 days. 3 days after addition of 5 μM naphthyl acetic acid, 4–5 g roots were ground in extraction buffer (50 mM HEPES pH7.5, 50 mM NaCl, 5 mM MgCl2, 10% glycerol, 0.5 mM PMSF, 100 μM GTP-γ-S and Complete EDTA-Free Protease Inhibitor (Roche), centrifuged and 1 mM DTSSP (3,3'-dithiobis-(sulfosuccinimidyl propionate)) was added to the supernatant, incubated on ice for 30 min, followed by quenching with Tris-HCl pH7.5 at 50 mM on ice for 10 min. Microsomes were pelleted onto a cushion of 2 M sucrose by centrifugation at 541,000 × g for 30 min at 4 °C and re-suspended in 1.8 ml extraction buffer with 2% CHAPS, and centrifuged at 541,000 × g for 30 min at 4 °C. 200 μl anti-GFP μMACS magnetic microbeads (Miltenyi Biotec) were added to the supernatant and incubated for 60 min on ice with gentle agitation. Bound proteins were eluted in 50 μl Laemmli protein loading buffer. Samples were separated on a NuPAGE Novex 4–12 Bis Tris polyacrylamide gel (Thermofisher Ltd).

The in-gel trypsin digestion and LC-MS/MS spectrometry were performed at the Central Proteomics Facility, University of Oxford (www.proteomics.ox.ac.uk) on three replicates per genotype. Ultra-performance liquid chromatography (UPLC) separation was performed on a Dionex Ultimate 3000 coupled to a Thermo Scientific Q-Exactive High Field Mass Spectrometer for tandem MS–MS

analysis. Samples were loaded onto a 10 cm long home packed column (Reprosil-Pur C18-Aq, 3-micron beads, Dr Maisch) over a 60 min gradient of 2–35% acetonitrile in 5% DMSO, 0.1% formic acid at a flow rate of 250 nl/min. MS1 scans were acquired at a resolution of 60,000 at 200 m/z with the top 12 most abundant precursors targeted for HCD fragmentation. Raw files from each injection were converted to a MASCOT Generic Format (MGF) and searched on the MASCOT server (version 2.5.1) against the UPR Arabidopsis Thaliana database (dated 2015/02/11). The search parameters allowed for 2 missed cleavages, a peptide mass tolerance of ±10 ppm with carbamidomethyl as a fixed modification on cysteine and oxidation (M) as a variable modification. Fragment mass tolerance was set to ±0.02 Da. Proteins were quantified using the label-free SInQ pipeline[71], with a q-value of ≤0.01 (corresponding to a 1% false discovery rate (FDR)), using only peptide spectrum matches with a q-value ≤ 0.01. Proteins that were not detected in all three replicates of the YFP:RAB-G3f immunoprecipitation were eliminated from the dataset. The remainder were ranked on their SIn values[71] in three ways: (i) by their abundance in the immunoprecipitate from untransformed plants (lowest to highest) then by their mean abundance in the YFP:RAB-G3f sample (highest to lowest); (ii) by dividing the value in the RAB-G3f dataset by the combined values for total microsomes and the untransformed sample; and (iii) by dividing the values for the YFP:RAB-G3f sample by the combined values for YFP:RAB-A2a and YFP:RAB-A5c. The rank position in each of the rankings (i–iii) were then summed and a final ranking was made on this sum (lowest to highest). Prior to ranking, zero values (protein undetected) were eliminated by adding half the value of the least abundant protein in the entire dataset to SIn value of every protein. Statistical analysis was performed using the PLGEM (power law general error method) on pairwise samples[71].

MAPK assays

Two weeks-old seedlings ($n = 12$) were placed in dH$_2$O for 16 h. 1 μM flg22 was added for 10 min and tissue (50 mg per sample) was shock frozen. To the grinded material 50 μL SDS-PAGE sample loading (0.35 M Tris-HCl pH 6.8; 30% [v/v] glycerol; 10% [v/v] SDS; 0.6 M dithiothreitol; and 0.012% [w/v] bromphenol blue) was added. Total proteins were separated by electrophoresis in 12% SDS-polyacrylamide gel and electrophoretically transferred to a polyvinylidene fluoride membrane according to the manufacturer's instructions (Bio-Rad). Transferred proteins were detected with Ponceau-S. Polyclonal primary antibodies against phospho-p44/42 MAPK (Cell Signaling Technologies) were used, with alkaline phosphatase-conjugated anti-rabbit as secondary antibodies. Signal detection was performed using CDPstar (Roche).

Autophagy assays

To investigate RABG3b, NET4A and NET4B involvement in autophagy, whole seedlings were grown in liquid ½ MS media (1% sucrose) in 12-well plates under continuous light and constant shaking at 80 rpm. For each genotype, treatment and time point 20 seedlings were grown. After 1 week, seedlings, except for mock, were treated with 10 μM flg22 for either 1 h or 2 h. Afterwards the first round of samples was harvested. The other set of samples underwent a recovery period of 8 h in ½ MS media containing 1 μM concanamycin A (conA) (CAS 80890-47-7; Santa Cruz), which has been dissolved in DMSO as a 2 mM stock solution, or DMSO (as control, same volume as conA). Since conA is light sensitive, seedlings (with and without conA) were subjected to dark treatment where plates were wrapped in aluminium foil. For all treatments, wells were first washed with 1 ml media containing respective treatment before incubation. Seedlings were harvested in microcentrifugation tubes containing a variety of different sized glass beads (2.85–3.45 mm, 1.7–2.1 mm and 0.75–1.00 mm; Lactan GmbH)

and flash frozen in liquid nitrogen. Plant tissue was grinded with mixer mill MM400 (3 × 30 s, 30 Hz; Retsch) and the proteins were extracted in 250 μl extraction buffer containing 100 mM Tris, 200 mM NaCl, 1 mM EDTA, 2% 2-Mercaptoethanol, 0,2% Triton X-100 and cOmplete, EDTA-free Protease Inhibitor Cocktail (SIGMA) with a pH of 7.8. Well mixed samples were centrifuged at 27.000 × g for 10 min at 4 °C. The whole supernatant was transferred and centrifuged again. 100 μl of resulting supernatant was eluted in 2x Laemmli protein loading buffer and boiled for 10 min at 95 °C. Protein amount was quantified via Amido black. 10 μl of sample was diluted in 190 μl water and 1 ml of Amido black staining solution (90% methanol, 10% acetic acid, 0.005% (w/v) Amido black 10B (SIGMA)) was added. For the staining solution a Bovine Serum Albumin (BSA) standard curve was determined. Samples were mixed thoroughly, centrifuged for 10 min at 27000 × g and the supernatant was discarded. Pellets were washed in 1 ml washing solution (90% ethanol and 10% acetic acid) and centrifuged again. After full removal of supernatant, samples were dissolved in 1 ml 0.2 N NaOH and 200 μl was loaded on 96-well plates suitable for a plate reader (Synergy™ HTX Multi-Mode Microplate Reader; Bio-Tek). Concentration was measured at 630 nm and calculated via the previously determined BSA standard curve where y stands for the measured optical density (OD) and x for the protein concentration. 15 μg of protein was loaded on 4–20% Mini-PROTEAN® TGX™ precast gel (Bio-Rad) and blotted on nitrocellulose membrane using the semi-dry Trans-Blot® Turbo™ Transfer System (Bio-Rad). Total protein extract was immunoblotted with either anti-NBR1 (1:2000; Agrisera), anti-Catalase (1:10000; Agrisera) or anti-ATG8a-i (1:4000; Agrisera) antibodies. Images were acquired by developing with SuperSignal™ West Pico PLUS Chemiluminescent Substrate (Thermo Fischer) and detected via ChemiDoc™ Touch Imaging System (Bio-Rad).

Actin co-sedimentation assays

The NET4B 1-105 aa NAB domain was Gateway-cloned into expression vector pGAT4, expressed as a 6xHis-tagged fusion protein in *E. coli* strain Rosetta 2 (DE3) pLysS (Novagen) and purified using Ni-NTA resin (Qiagen) according to manufacturer"s instructions. Recombinant proteins were dialysed into reaction buffer (4 mM Tris pH 8.0, 0.2 mM DTT, 0.4 mM ATP, 20 mM KCl, 4 mM imidazole, 2 mM EGTA, 0.4 mM MgSO4). Rabbit muscle actin (Cytoskeleton Inc.) in G-buffer (2 mM Tris pH 8.0, 0.5 mM DTT, 0.2 mM CaCl2, 0.2 mM ATP) was polymerized by the addition of 10 x KME (500 mM KCl, 10 mM MgSO4, 10 mM EGTA, 100 mM imidazole, pH 6.5). Actin (5um) and NET4B (10 μM) were mixed in reaction buffer at room temperature for 1 hr and then centrifuged at 350,000 × g for 15 min before supernatant and pellet fractions were compared using SDS-PAGE.

Confocal microscopy

Confocal microscopy was performed on either a Zeiss 880 LSM with Airyscan detector module a, or Leica SP5 TCS confocal laser scanning microscope equipped with a 63x water or oil immersion objective. Leaf or root samples were mounted in water. Large root areas were acquired in tile scan mode with auto stitching. For *N. benthamiana* imaging, small sections were excised from the leaf and mounted on slides in water. Roots of stable Arabidopsis lines were mounted on slides in ½ MS with the green tissues free outside the coverslip chamber. Where multiple fluorescent proteins or markers were co-imaged, data was acquired sequentially in multitrack or multichannel mode with laser line switching. GFP and BCECF were excited using the 488-nm argon laser, and fluorescence emission captured between 500 and 550 nm for GFP, between 580 and 620 nm for FM4-64 and between 510 and 550 nm for BCECF. RFP was excited at 561 nm, and emission captured between 580 and 620 nm.

mCherry was excited at 594 and emission captured 600–650 nm. mTAGBFP2 was excited with a 405 nm laser and emission captured 410 nm–470 nm. MDY-64 was excited with a 458 nm laser and emitted light imaged using an Airyscan detector with a BP 495–550 nm filter.

Forster resonance energy transfer-fluorescence lifetime imaging microscopy (FRET-FLIM) experiments were performed on a Leica SP5 TCS SMD confocal microscope with a Picoquant LSM FLIM upgrade kit. *N. benthamiana* leaves were transiently transformed by Agrobacterium infiltration with both NET4A-GFP and NET4B-RFP constructs. FLIM experimentation and analysis using PicoQuant SymPhoTime 32 software was carried as described in[72]. All measurements were taken from whole-field images of cells expressing fluorophore fusion proteins at similar level, and at least 6 measurements were taken for each analysis.

Actin imaging and quantification
Leaf discs (approx. 4 mm width) of 4 weeks-old soil grown plants were submerged in stomata opening buffer (10 mM 2-(N-morpholino)-ethanesulfonic acid (MES) pH 6.1, 50 mm KCl, 10 μm CaCl2, 0.01% Tween) and incubated in the light for 2 h. Subsequently, the leaf discs were transferred into stomata assay buffer supplemented with 20 μm flg22, and incubated in the light for a further 1 or 2 hrs before imaging. Super-resolution Lifeact labelled actin arrays within guard cells were imaged using a Zeiss 880 LSM with Airyscan detector module (Excitation 488 nm, emission 495 nm–550 nm). The actin orientation within z stacks (Mean angular difference and Parallelness) was quantified in ImageJ using the LPIXEL Inc (https://lpixel.net/en/products/lpixel-imagej-plugins/) set analysis of tools as previously described[13,28,73,74]. Briefly, a maximum intensity projection was created from each Z stack which was then rotated so that the long axis of the guard cell was vertical. The maximum intensity projection of the stoma was then separated into individual guard cells. Using the freehand selection tool, the guard cell was outlined to create an ROI, which was subsequently added to the ROI manager. The cell medial axis (angle) was calculated in the ROI manager for each guard (using the "Fit Ellipse" option under "Set Measurements.") The LPX Filter2d plugin, using the filter "lineFilters" and the linemode "lineExtract," was used to skeletonize actin in each guard cell. The default settings for "lineExtract" were used (giwslter = 5, mdnmsLen = 15, shaveLen = 5, delLen = 5, preGauss = −1). Skeletonised filaments from surrounding cells were excluded from analysis by loading the guard cell ROI and using "clear outside". The average theta and parallelness for each guard cell were calculated using the LPX Filter2d plugin, using the filter "lineFilters" and the linemode "lineFeature." The mean angular difference was calculated by subtracting the angle of the cell medial axis over the horizontal (close to 90°) from the average theta and taking the absolute value.

BCECF staining
To stain the vacuolar lumen of *A. thaliana* guard cells, the pH-sensitive dye BCECF-AM (Molecular Probes) was used. BCECF was prepared as a 1 mg/mL stock solution (-1.67 mM) in DMSO. Leaf discs (4 mm width) of 3 weeks-old soil grown plants were submerged in stomata assay buffer (10 mM 2-(N-morpholino)-ethanesulfonic acid (MES) pH 6.1, 50 mm KCl, 10 μm CaCl2, 0.01% Tween) and incubated in the light for 2 h. Subsequently, the leaf discs were transferred into stomata assay buffer supplemented with the respective elicitors, and incubated in the light for further 2 h. 90 min into the treatment, BCECF stock solution was added to a final concentration of 10 μM. After 30 min of dye loading the leaf discs were imaged using a confocal microscope, leaf discs were washed twice in stomata assay buffer before imaging. Airyscan confocal z stacks of guard cell vacuoles loaded with BCECF were surface rendered and their volume quantified using Fiji with 3D Viewer plugin[49,50]. Volumes were also confirmed by segmentation and volume quantification with Amira for Life & Biomedical Sciences (Thermo Scientific).

MDY-64 staining
Leaf sections were incubated in 0.25 μm MDY-64 in 1/2 MS for 10 min in darkness. These sections were then washed and mounted in fresh 1/2 MS and imaged by confocal microscopy.

Immunogold labelling and transmission electron microscopy
A NET4B fragment (residues 121-220) was expressed as a His-tagged, recombinant protein and purified using Ni-NTA resin (Qiagen). Polyclonal antibodies were raised in mice as described in[1]. Distal 1–2 mm root tips of 7 days-old Arabidopsis Col-0 seedlings were excised and immersed in 20% (w/v) BSA, and immediately high-pressure frozen with a Leica EMPACT high- pressure freezer. Samples were fixed by freeze substitution with a Leica EM automated freeze substitution (AFS) device (Leica Microsystems GmbH) using anhydrous acetone containing 0.25% (v/v) glutaraldehyde and 0.1% (w/v) uranyl acetate. Resin was gradually infiltrated (Monostep Lowicryl HM20 Agar Scientific) replacing acetone, polymerised and ultrathin sections (50–70 nm) prepared. Sections were rinsed with 0.1% (v/v) glycine PBS, blocked for 30 min in 1% (w/v) BSA PBS and finally incubated in 0.1% BSA-c (Aurion) PBS. Sections were incubated for 30 min with the primary antibody (rabbit anti-NET4B) or the pre-bleed sera as a negative control. Grids were washed in 0.1% BSA-c and then incubated for 30 min with the 5 nm colloidal gold-conjugated goat anti-rabbit secondary antibody (British Biocell International, Cardiff, UK). Sections were also incubated without the secondary antibody as a negative control for immunogold labelling (secondary omission control). The grids were rinsed in PBS and the antigen-antibody-gold complex stabilised by incubation in 1% (v/v) glutaraldehyde in PBS. Sections were imaged using a Hitachi H-7600 TEM operating at 100 kV fitted with an AMT Orca-ER digital camera (Advanced Microscopy Techniques, Danvers, USA). Quantification of tonoplast labelling was carried out using the Relative Labelling Index (RLI) method (Mayhew, Lucocq and Griffiths, 2002) (Mayhew and Lucocq, 2008). The tonoplast demonstrated the most abundant anti-NET4B labelling satisfying both criteria for preferential labelling giving a RLI of 3.58, and a Chi squared 70.34% of total.

Statistical analysis
Mann Whitney *t*-test, 2-way ANOVA multiple comparisons, and ANOVA with Bonferroni's Multiple comparison test were performed using GraphPad Prism, GraphPad Software, San Diego, California USA, www.graphpad.com

Reporting summary
Further information on research design is available in the Nature Portfolio Reporting Summary linked to this article.

Data availability
All data and materials generated will be made freely available to the research community. Biological materials can be obtained upon request. Source data are provided with this paper. The mass spectrometry proteomics data have been deposited to the ProteomeXchange Consortium via the PRIDE partner repository with the dataset identifier PXD044263 and the identifier PXD044681. Source data are provided with this paper.

References

1. Deeks, M. J. et al. A superfamily of actin-binding proteins at the actin-membrane nexus of higher plants. *Curr. Biol.* **22**, 1595–1600 (2012).

2. Wang, P., Hawkins, T. J. & Hussey, P. J. Connecting membranes to the actin cytoskeleton. *Curr. Opin. Plant Biol.* **40**, 71–76 (2017).

3. Hawkins, T. J., Deeks, M. J., Wang, P. & Hussey, P. J. The evolution of the actin binding NET superfamily. *Front. Plant Sci.* **5**, 254 (2014).

4. Wang, P. & Hussey, P. J. NETWORKED 3B: a novel protein in the actin cytoskeleton-endoplasmic reticulum interaction. *J. Exp. Botany* **68**, 1441–1450 (2017).

5. Duckney, P. et al. Actin-membrane interactions mediated by NET-WORKED2 in Arabidopsis pollen tubes through associations with Pollen Receptor-Like Kinase 4 and 5. *New Phytol.* **216**, 1170–1180 (2017).

6. Duckney, P. et al. NETWORKED2-subfamily proteins regulate the cortical actin cytoskeleton of growing pollen tubes and polarised pollen tube growth. *New Phytol.* **231**, 152–164 (2021).

7. Zang, J. et al. A novel plant actin-microtubule bridging complex regulates cytoskeletal and ER structure at ER-PM contact sites. *Curr. Biol.* **31**, 1251–1260.e4 (2021).

8. Zang, J., Zhang, T., Hussey, P. J. & Wang, P. Light microscopy of the endoplasmic reticulum–membrane contact sites in plants. *J. Microsc.* **280**, 134–139 (2020).

9. Wang, P. et al. Plant AtEH/Pan1 proteins drive autophagosome formation at ER-PM contact sites with actin and endocytic machinery. *Nat. Commun.* **10**, 1–16 (2019).

10. Scheuring, D. et al. Actin-dependent vacuolar occupancy of the cell determines auxin-induced growth repression. *Proc. Natl Acad. Sci. USA* **113**, 452–457 (2016).

11. Kaiser, S., Eisa, A., Kleine-Vehn, J. & Scheuring, D. NET4 modulates the compactness of vacuoles in *Arabidopsis thaliana*. *Int. J. Mol. Sci.* **20**, 4752 (2019).

12. Tanaka, Y. et al. Intra-vacuolar reserves of membranes during stomatal closure: the possible role of guard cell vacuoles estimated by 3-D reconstruction. *Plant Cell Physiol.* **48**, 1159–1169 (2007).

13. Higaki, T., Kutsuna, N., Sano, T., Kondo, N. & Hasezawa, S. Quantification and cluster analysis of actin cytoskeletal structures in plant cells: role of actin bundling in stomatal movement during diurnal cycles in Arabidopsis guard cells. *Plant J.* **61**, 156–165 (2010).

14. Kim, M., Hepler, P. K., Eun, S. O., Ha, K. S. & Lee, Y. Actin filaments in mature guard cells are radially distributed and involved in stomatal movement. *Plant Physiol.* **109**, 1077–1084 (1995).

15. MacRobbie, E. A. C. & Kurup, S. Signalling mechanisms in the regulation of vacuolar ion release in guard cells. *New Phytol.* **175**, 630–640 (2007).

16. Dong, C. H. et al. ADF proteins are involved in the control of flowering and regulate f-actin organization, cell expansion, and organ growth in arabidopsis. *Plant Cell* **13**, 1333–1346 (2001).

17. Lemichez, E. et al. Inactivation of AtRac1 by abscisic acid is essential for stomatal closure. *Genes Develop.* **15**, 1808–1816 (2001).

18. McLachlan, D. H., Kopischke, M. & Robatzek, S. Gate control: Guard cell regulation by microbial stress. *New Phytol.* **203**, 1049–1063 (2014).

19. Beck, M. et al. Expression patterns of FLAGELLIN SENSING 2 map to bacterial entry sites in plant shoots and roots. *J. Exp. Botany* **65**, 6487–6498 (2014).

20. Boutrot, F. & Zipfel, C. Function, discovery, and exploitation of plant pattern recognition receptors for broad-spectrum disease resistance. *Ann. Rev. Phytopathol.* **55**, 257–286 (2017).

21. Couto, D. & Zipfel, C. Regulation of pattern recognition receptor signalling in plants. *Nat. Rev. Immunol.* **16**, 537–552 (2016).

22. Liu, Y. et al. Anion channel SLAH3 is a regulatory target of chitin receptor-associated kinase PBL27 in microbial stomatal closure. *eLife* **8**, e44474 (2019).

23. Henty-Ridilla, J. L. et al. The plant actin cytoskeleton responds to signals from microbe-associated molecular patterns. *PLoS Pathogens* **9**, e1003290 (2013).

24. Henty-Ridilla, J. L., Li, J., Day, B. & Staiger, C. J. Actin depolymerizing factor 4 regulates actin dynamics during innate immune signaling in Arabidopsis. *Plant Cell* **26**, 340–352 (2014).

25. Zou, M. et al. MPK3- and MPK6-mediated VLN3 phosphorylation regulates actin dynamics during stomatal immunity in Arabidopsis. *Nat. Commun.* **12**, 6474 (2021).

26. Ebine, K. et al. Plant vacuolar trafficking occurs through distinctly regulated pathways. *Curr. Biol.* **24**, 1375–1382 (2014).

27. Löfke, C., Dünser, K., Scheuring, D. & Kleine-Vehn, J. Auxin regulates SNARE-dependent vacuolar morphology restricting cell size. *eLife* **4**, e05868 (2015).

28. Shimono, M. et al. Quantitative evaluation of stomatal cytoskeletal patterns during the activation of immune signaling in *Arabidopsis thaliana*. *PloS ONE* **11**, e0159291 (2016).

29. Pedrazzini, E., Komarova, N. Y., Rentsch, D. & Vitale, A. Traffic routes and signals for the tonoplast. *Traffic* **14**, 622–628 (2013).

30. Zhen, Y. & Stenmark, H. Cellular functions of Rab GTPases at a glance. *J. Cell Sci.* **128**, 3171–3176 (2015).

31. Bourdais, G. et al. The use of quantitative imaging to investigate regulators of membrane trafficking in Arabidopsis stomatal closure. *Traffic* (2019) https://doi.org/10.1111/tra.12625.

32. Pereira-Leal, J. B. & Seabra, M. C. Evolution of the Rab family of small GTP-binding proteins. *J. Mol. Biol.* **313**, 889–901 (2001).

33. Rutherford, S. & Moore, I. The Arabidopsis Rab GTPase family: another enigma variation. *Curr. Opin. Plant Biol.* **5**, 518–528 (2002).

34. Beck, M., Zhou, J., Faulkner, C., Mac, D. & Robatzek, S. Spatio-temporal cellular dynamics of the Arabidopsis flagellin receptor reveal activation status-dependent endosomal sorting. *Plant Cell* **24**, 4205–4219 (2012).

35. Spallek, T. et al. ESCRT-I Mediates FLS2 endosomal sorting and plant immunity. *PLoS Genetics* **9**, e1004035 (2013).

36. Mbengue, M. et al. Clathrin-dependent endocytosis is required for immunity mediated by pattern recognition receptor kinases. *Proc. Natl Acad. Sci. USA* **113**, 11034–11039 (2016).

37. Smith, J. M., Salamango, D. J., Leslie, M. E., Collins, C. A. & Heese, A. Sensitivity to flg22 is modulated by ligand-induced degradation and de novo synthesis of the endogenous flagellin-receptor FLA-GELLIN-SENSING2. *Plant Physiol.* **164**, 440–454 (2014).

38. Kwon, S. I., Cho, H. J., Kim, S. R. & Park, O. K. The Rab GTPase RabG3b positively regulates autophagy and immunity-associated hypersensitive cell death in Arabidopsis. *Plant Physiol.* **161**, 1722–1736 (2013).

39. Kwon, S. I. et al. The Rab GTPase RabG3b functions in autophagy and contributes to tracheary element differentiation in Arabidopsis. *Plant J.* **64**, 151–164 (2010).

40. Yang, F. et al. A plant immune receptor degraded by selective autophagy. *Mol. Plant* **12**, 113–123 (2019).

41. Yamauchi, S. et al. Autophagy controls reactive oxygen species homeostasis in guard cells that is essential for stomatal opening. *Proc. Natl Acad. Sci. USA* **116**, 19187–19192 (2019).

42. Yoshii, S. R. & Mizushima, N. Monitoring and measuring autophagy. *Int. J. Mol. Sci.* **18**, 1865 (2017).

43. Zaffagnini, G. & Martens, S. Mechanisms of selective autophagy. *J. Mol. Biol.* **428**, 1714–1724 (2016).

44. Merkulova, E. A. et al. Assessment and optimization of autophagy monitoring methods in arabidopsis roots indicate direct fusion of autophagosomes with vacuoles. *Plant Cell Physiol.* **55**, 715–726 (2014).

45. Thompson, A. R., Doelling, J. H., Suttangkakul, A. & Vierstra, R. D. Autophagic nutrient recycling in Arabidopsis directed by the ATG8 and ATG12 conjugation pathways. *Plant Physiol.* **138**, 2097–2110 (2005).

46. Cui, Y. et al. Activation of the Rab7 GTPase by the MON1-CCZ1 complex is essential for PVC-to-vacuole trafficking and plant growth in Arabidopsis. *Plant Cell* **26**, 2080–2097 (2014).

47. Geldner, N. et al. Rapid, combinatorial analysis of membrane compartments in intact plants with a multicolor marker set. *Plant J.* **59**, 169–178 (2009).

48. Scheuring, D., Schöller, M., Kleine-Vehn, J. & Löfke, C. Vacuolar staining methods in plant cells. *Methods Mol. Biol.* **1242**, 83–92 (2015).

49. Schmid, B., Schindelin, J., Cardona, A., Longair, M. & Heisenberg, M. A high-level 3D visualization API for Java and ImageJ. *BMC Bioinform.* **11**, 1–7 (2010).

50. Viotti, C. et al. The endoplasmic reticulum is the main membrane source for biogenesis of the lytic vacuole in Arabidopsis. *Plant Cell* **25**, 3434 (2013).

51. Li, P. & Day, B. Battlefield cytoskeleton: turning the tide on plant immunity. *Mol. Plant-Microbe Interact.* **32**, 25–34 (2019).

52. Kadota, Y. et al. Direct regulation of the NADPH Oxidase RBOHD by the PRR-associated kinase bik1 during plant immunity. *Mol. Cell* **54**, 43–55 (2014).

53. Boudsocq, M. et al. Differential innate immune signalling via Ca 2+ sensor protein kinases. *Nature* **464**, 418–422 (2010).

54. Lu, Y. J. et al. Arabidopsis calcium-dependent protein kinase 3 regulates actin cytoskeleton organization and immunity. *Nat. Commun.* **11**, 1–12 (2020).

55. Lin, X. et al. Tyrosine phosphorylation of Rab7 by Src kinase. *Cell. Signall.* **35**, 84–94 (2017).

56. Kang, Y. et al. HopW1 from *Pseudomonas syringae* disrupts the actin cytoskeleton to promote virulence in Arabidopsis. *PLoS Pathogens* **10**, 1004232 (2014).

57. Bray Speth, E., Imboden, L., Hauck, P. & He, S. Y. Subcellular localization and functional analysis of the Arabidopsis GTPase RabE. *Plant Physiol.* **149**, 1824–1837 (2009).

58. Shimono, M. et al. The Pseudomonas syringae type III effector HopG1 induces actin remodeling to promote symptom development and susceptibility during infection. *Plant Physiol.* **171**, 2239–2255 (2016).

59. Tomczynska, I., Stumpe, M. & Mauch, F. A conserved RxLR effector interacts with host RABA-type GTPases to inhibit vesicle-mediated secretion of antimicrobial proteins. *Plant J.* **95**, 187–203 (2018).

60. Thor, K. et al. The calcium-permeable channel OSCA1.3 regulates plant stomatal immunity. *Nature* **585**, 569–573 (2020).

61. Göhre, V. et al. Plant pattern-recognition receptor FLS2 is directed for degradation by the bacterial ubiquitin ligase AvrPtoB. *Curr. Biol.* **18**, 1824–1832 (2008).

62. Grefen, C. et al. A ubiquitin-10 promoter-based vector set for fluorescent protein tagging facilitates temporal stability and native protein distribution in transient and stable expression studies. *Plant J.* **64**, 355–365 (2010).

63. Zhang, X., Henriques, R., Lin, S.-S., Niu, Q.-W. & Chua, N.-H. Agrobacterium-mediated transformation of *Arabidopsis thaliana* using the floral dip method. *Nat. Protocols* **1**, 641–646 (2006).

64. Voigt, B. et al. GFP-FABD2 fusion construct allows in vivo visualization of the dynamic actin cytoskeleton in all cells of Arabidopsis seedlings. *Eur. J. Cell Biol.* **84**, 595–608 (2005).

65. Fu, C. et al. Hot Fusion: an efficient method to clone multiple DNA fragments as well as inverted repeats without ligase. *PLoS One* **9**, e115318 (2014).

66. CA, S., WS, R. & KW, E. NIH Image to ImageJ: 25 years of image analysis. *Nat. Methods* **9**, 671–675 (2012).

67. Mersmann, S., Bourdais, G., Rietz, S. & Robatzek, S. Ethylene signaling regulates accumulation of the FLS2 receptor and is required for the oxidative burst contributing to plant immunity. *Plant Physiol.* **154**, 391–400 (2010).

68. Bourdais, G. et al. Large-scale phenomics identifies primary and fine-tuning roles for CRKs in responses related to oxidative stress. *PLoS Genet.* **11**, e1005373 (2015).

69. Schmittgen, T. D. & Livak, K. J. Analyzing real-time PCR data by the comparative C(T) method. *Nat. Protoc.* **3**, 1101–1108 (2008).

70. Van Leene, J. et al. An improved toolbox to unravel the plant cellular machinery by tandem affinity purification of Arabidopsis protein complexes. *Nat. Protoc.* **10**, 169–187 (2015).

71. Trudgian, D. C. et al. Comparative evaluation of label-free SINQ normalized spectral index quantitation in the central proteomics facilities pipeline. *Proteomics* **11**, 2790–2797 (2011).

72. Wang, P. et al. The plant cytoskeleton, NET3C, and VAP27 mediate the link between the plasma membrane and endoplasmic reticulum. *Curr. Biol.* **24**, 1397–1405 (2014).

73. Biel, A., Moser, M. & Meier, I. A role for plant KASH proteins in regulating stomatal dynamics. *Plant Physiol.* **182**, 1100–1113 (2020).

74. Higaki, T. Quantitative evaluation of cytoskeletal organizations by microscopic image analysis. *Plant Morphol.* **29**, 15–21 (2017).

Author contributions

P.J.H. and S.R. conceived the project and supervised the research. T.J.H., M.Ko., P.J.D., K.R., D.A.M, J.T.M.K., G.D.J., M.Ka., I.M., Y.D., P.J.H., and S.R. designed the methodology; T.J.H., M.Ko., P.J.D., K.R., D.A.M., J.T.M.K., M.T.B., A.C.R., M.C., A.A., G.D.J., M.Ka. performed research; T.J.H., M.Ko., P.J.D., K.R., D.A.M., J.T.M.K., M.T.B., A.C.R., G.D.J., M.Ka., I.M., Y.D., P.J.H., and S.R. analysed data; S.R. and T.J.H. wrote the paper with edits from P.J.H., K.R., and P.J.D.

Competing interests

The authors have no competing interests.

Additional information

Supplementary information The online version contains supplementary material available at https://doi.org/10.1038/s41467-023-41337-z.

Correspondence and requests for materials should be addressed to Patrick J. Hussey or Silke Robatzek.

Peer review information *Nature Communications* thanks the anonymous reviewer(s) for their contribution to the peer review of this work.

Reprints and permissions information is available at http://www.nature.com/reprints

Publisher's note Springer Nature remains neutral with regard to jurisdictional claims in published maps and institutional affiliations.